Received: 30 August 2018 | Revised: 21 November 2018 | Accepted: 8 January 2019

DOI: 10.1002/stc.2331

RESEARCH ARTICLE

WILEY

Effects of the long-term behaviour of isolation devices on the seismic response of base-isolated buildings

Fabio Mazza

Dipartimento di Ingegneria Civile, Università della Calabria, Rende (Cosenza), Italy

Correspondence
Fabio Mazza, Dipartimento di Ingegneria Civile, Università della Calabria, Rende (CS) 87036, Italy.
Email: fabio.mazza@unical.it

Funding information
Re.L.U.I.S.

Summary

Seismic isolation is widely used around the world for the protection of buildings, but its long-term behaviour was not considered in detail in past seismic design of isolated structures. Nevertheless, the American seismic code has recently introduced an explicit procedure aimed at evaluating upper-bound and lower-bound values of isolation system properties. Yet there are few studies on the evolution and extent of the deterioration of elastomeric (e.g., high-damping rubber bearings) and sliding (e.g., flat sliding bearings) isolators during their lifetime and on their impact on the seismic behaviour of the superstructure. To investigate this problem, six-storey–reinforced concrete buildings, base isolated with high-damping rubber bearings acting alone or in combination with flat sliding bearings, are designed without considering the variability of mechanical properties of the isolation system due to ageing and air temperature. Then, based on experimental results from accelerated ageing tests at high temperature, mathematical models are implemented to account for oxidation of elastomers and friction changes. The variability of mechanical properties at different mean temperatures, due to seasonal thermal variations, is also considered. Finally, fragility curves are developed for the base-isolation system and superstructure on the basis of nonlinear dynamic analysis of the degraded test structures.

KEYWORDS

ageing effects, air temperature effects, elastomeric bearings, fragility curves, nonlinear seismic analysis, sliding bearings

1 | INTRODUCTION

Base-isolation technique has long been used worldwide for the seismic protection of public and residential buildings, but seismic codes generally do not take into account ageing and environmental effects on degradation of the mechanical properties of the isolation devices. The introduction of the property modification factor approach to bound the likely seismic response of isolators has first been applied in the American code for new buildings,[1] whereas a similar approach is implemented in the European code for bridges.[2] In detail, maximum or minimum factors for each type of event (e.g., ageing, air temperature, and variations observed during testing) and an adjustment factor, taking into account the reduced probability of cumulative effects during an earthquake, are multiplied in order to define upper- and lower-bound force–displacement laws. However, other codes (e.g., the Italian code[3]) are limited to establish the maximum variation of the mechanical properties of the isolators, vis-à-vis the corresponding nominal values, only for the purpose of

qualification tests. Finally, the long-term behaviour of the isolation system is explicitly taken into account during the design process in Japan, requiring that the manufacturers of the isolators provide the degree of variation of the main design parameters as function of ageing and environmental effects.[4] During the lifetime of the elastomeric (e.g., high-damping rubber bearings [HDRBs]) and sliding (e.g., flat sliding bearings [FSBs]) bearings, representing some of the most widely used types of isolation systems, ageing and air temperature are important factors that affect the degradation of rubber and friction coefficient of the sliding surface, respectively. The mechanical properties of the HDRBs change uniformly along the radial direction of the isolator in a relatively short time, until a stable equilibrium state is reached in the inner region bounded by an external critical depth,[5] the latter being an exponential function of the temperature.[6] The outer region is also affected by an oxidation process, related to time and depending on the amount of oxygen, which produces a degradation of properties whose effects diminish moving towards the critical depth. Moreover, the HDRBs considerably increase their horizontal and vertical stiffnesses for decreasing values of the air temperature through rubber crystallization due to prolonged exposure to cold weather, whereas their cyclic behaviour does not change significantly at high air temperatures.[7] Finally, it should be noted that ageing[8,9] and air temperature[10] do not affect the equivalent viscous damping ratio of the HDRBs significantly. On the other hand, the friction coefficient of the FSBs presents an age-related increase that can be considered because of changes in the adhesive properties depending on creep of materials and subsequent increase in the contact area between the sliding pad and sliding plate.[11] In particular, creep affects the static friction coefficient during lifetime of the isolator whereas at the onset, the dynamic friction coefficient remains almost unchanged. Air temperature also plays a not negligible role on the friction coefficient,[12] with a rate of reduction greater when passing from low-to-medium values than from medium-to-high values.[13] However, the significant frictional heating during seismic loading moderates the effects of low temperatures at the sliding interface that combined with isolators placed in normal environment obviates the air temperature effects on the friction coefficient.[14] Although the analytical and experimental studies above-mentioned have provided considerable insight into how to predict the long-term behaviour of elastomeric and sliding bearings when subjected to ageing and air temperature effects, more investigation is required to evaluate the effects of these phenomena on the nonlinear seismic analysis of base-isolated buildings.

Design procedures of the base-isolation systems proposed by international seismic codes generally allow for the use of simplified models to describe the hysteretic response of elastomeric and sliding bearings, in line with commercial software generally assuming properties of the bearings constant during an earthquake. Conversely, the use of a simple but reasonably accurate model is required to take into account the experimentally observed behaviour of the HDRBs and FSBs. In detail, the HDRBs behave nonlinearly, with horizontal stiffness decreasing with increasing vertical load and vertical stiffness decreasing with increasing lateral deformation.[15,16] Moreover, increasing values of horizontal displacement induce a reduction in both critical buckling load[17] and horizontal stiffness.[18] On the other hand, experimental studies have highlighted the complex nonlinear behaviour of the FSBs. The dynamic friction coefficient monotonically increases by an exponential law with the sliding velocity up to a constant value.[19] The axial pressure significantly reduces the high-velocity (i.e., dynamic fast) value of the friction coefficient, whereas the low-velocity (i.e., dynamic low) value is relatively unaffected.[20-22] Finally, the response of the FSBs shifts between the sticking and sliding phases, at the breakaway and motion reversals, highlighting a static friction coefficient greater than the dynamic one.[23]

A few studies on the effects of ageing on isolation systems[24–26] after 20, 30, and 40 years of use have been carried out, as well as recent numerical investigations[27-29] introducing modification factors accounting for ageing and air temperature effects. The aim of the present work is to investigate the effects of variability of the mechanical properties of elastomeric and sliding bearings, both during the design life and seismic motion, on the nonlinear dynamic response of base-isolated reinforced concrete (r.c.) structures. This study is also devoted to investigate the level of reliability of the property modification factor approach adopted in some advanced international seismic codes in predicting, conservatively, the nonlinear seismic response of base-isolation system and superstructure. In light of the evidence of previously described phenomena, attention is focused on ageing and air temperature effects, generally neglected in the design stage, combined with changes of the force-displacement laws due to the loading history. As a comparison, the property modification factors of bearing properties[1] proposed by American Society of Civil Engineers (ASCE 7-2016) are also applied to define the isolation system properties that are used in upper- and lower-bound analyses. First, six-storey r.c. framed structures, base isolated with HDRBs acting alone or in combination with FSBs, are designed in accordance with the current Italian code[2] in a high-risk seismic zone, considering nominal values of mechanical properties of the isolation system. More specifically, nine structural configurations are examined, combining three elastomer compounds of HDRBs (i.e., soft, normal, and hard) and two sliding friction coefficients of FSBs (i.e., low and medium). Then, a computer code is implemented for the nonlinear seismic analysis of the test structures, considering a lumped

plasticity model to describe the inelastic deformation of r.c. frame members of the superstructure,[30] whereas advanced nonlinear force-displacement laws are adopted for the isolation systems. The results of nonlinear time-history analysis are used to build fragility curves based on simple regression in the logarithmic space of structural response versus seismic intensity,[31] considering ground motions selected from the Pacific Earthquake Engineering Research Center database[32] and scaled in line with the design hypotheses adopted.

2 | MODELLING OF THE ISOLATION SYSTEM

2.1 | Time-dependent effects: Ageing

Mechanical properties of the HDRBs inevitably change over time and tend to cause an increase of the horizontal and vertical stiffnesses, with a reduction of the fundamental vibration periods that may affect the seismic response of a base-isolated structure. Ageing is dependent on the rubber compound and improper vulcanization and substantially increases for either very high damping or very low shear modulus.[33] Assuming linear material behaviour, the nominal horizontal (K_{H0}) and vertical (K_{V0}) stiffnesses of an HDRB can be evaluated as function of the initial (unaged) shear (G_0) and axial (E_0) moduli.

$$K_{H0} = \frac{G_0 \cdot A}{t_r} = \frac{G_0 \cdot \pi \cdot D^2}{4 \cdot t_r};\ K_{V0} = \frac{E_0 \cdot A}{t_r} = \frac{E_0 \cdot \pi \cdot D^2}{4 \cdot t_r} \tag{1ab}$$

A and D being the cross-sectional area and the diameter of a circular bearing, respectively, and t_r the total thickness of the rubber. The ageing depends on chemical reactions and diffusion rate of oxygen and is characterized by a fast stage during which the mechanical properties change almost uniformly over the whole area and a slow stage governed by oxidation of the external part until a critical depth.[5]

$$d^* = \alpha \cdot e^{\beta/T}, \tag{2}$$

increasing for lower values of air temperature,[34] where coefficients $\alpha(=1.2 \times 10^{-4}$ mm) and $\beta(=3.82 \times 10^3$ K$^{-1})$ can be evaluated with thermal oxidation tests.[8] That is why the aged shear modulus ($G(t)$) depends on the position inside the bearing and the horizontal stiffness can be expressed as

$$K_H(t) = \frac{Q_H(t)}{t_r}, \tag{3}$$

having

$$Q_H(t) = \int G_{aged} \cdot dA = G_0 \cdot \int_0^{2\pi} \int_0^{D/2} f(r, \theta) \cdot dr \cdot d\theta, \tag{4}$$

where $f(r, \theta)$ is a function describing the spatial variability of the shear modulus because of ageing. More specifically, Equation (4) can be divided in internal

$$Q_{Hi}(t) = 2 \cdot \pi \cdot G_0 \cdot \int_0^{R - d^*} (1 + \Delta f_{\text{fast}}) \cdot r \cdot dr, \tag{5a}$$

and external

$$Q_{He}(t) = 2 \cdot \pi \cdot G_0 \cdot \int_{R - d^*}^{R} \left[1 + \Delta f_{fast} + w(r) \cdot \Delta f_{slow}\right] \cdot r \cdot dr, \tag{5b}$$

contributions calculated on the corresponding reduced circular areas. In detail, fast and slow increases of the initial shear modulus are governed by the following expressions.[8]

$$\Delta f_{\text{fast}} = 88.4 \cdot e^{-1887.2/T}, \tag{6a}$$

$$\Delta f_{\text{slow}} = 9.3 \times 10^{-4} \cdot t_{ref}, \tag{6b}$$

where t_{ref} is the equivalent ageing time (expressed in days) at the reference temperature T_{ref} (expressed in degree Kelvin) of accelerated ageing tests whereas T represents the temperature under the service condition. It should be noted that constant parameters of Equation 6a6b are assumed equal to the values proposed by Paramashanti et al[8] on the basis of investigation on different rubber compounds. Moreover, a parabolic law

$$w(r) = \left(\frac{R - r - d^*}{d^*}\right)^2, \tag{7}$$

with the boundary conditions

$$w\left(r = R - d^*\right) = 0;\ w'\left(r = R - d^*\right) = \left(\partial w/\partial r\right)_{r=R-d^*} = 0;\ w(r = R) = 1, \tag{8abc}$$

describes the spatial variation of Δf_{slow} in the external part of a circular bearing with radius R. Finally, an equivalent aged shear modulus can be evaluated for each elastomer compound as

$$G(t) = \frac{K_H(t)}{K_{H0}} \cdot G_0, \tag{9}$$

by which an equivalent aged axial modulus can be assessed

$$E(t) = \left(\frac{1}{6 \cdot G(t) \cdot S_1^2} + \frac{4}{3 \cdot E_b}\right)^{-1}, \tag{10}$$

where E_b represents the volumetric compression modulus of the rubber (e.g., E_b = 2,000 MPa), whose variation over time is neglected, and $S_1 = D/(4t)$ is the primary shape factor, t being the thickness of the single layer of elastomer. Finally, the corresponding vertical stiffness is

$$K_V(t) = E(t) \cdot A / t_r. \tag{11}$$

On the other hand, time variation of the static friction coefficient during the stick–slip phases has been experimentally studied through durability tests,[11] highlighting an increase attributed primarily to creep of the materials and a corresponding increase in the contact area between sliding pad and sliding plate; moreover, negligible changes of the dynamic friction coefficient have been observed. Specifically, the following expression has been proposed to represent variability of the static friction coefficient over time:

$$\mu_s(t) = \mu_{s0} + 0.016 \cdot t^{0.1}, \tag{12}$$

where μ_{s0} is the initial (unaged) value of the static friction whereas t is the age, measured in years.

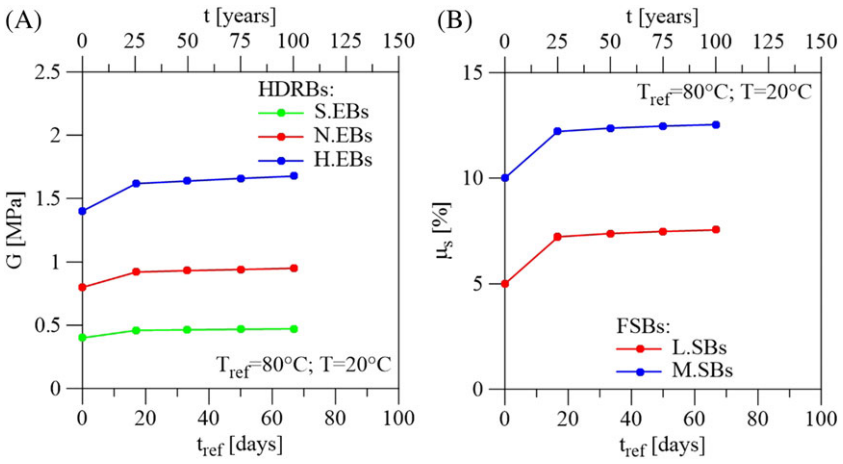

FIGURE 1 Effects of ageing on mechanical properties of the isolation system. (a) High-damping rubber bearings. (b) Flat sliding bearings

In line with international codes (e.g., American Society for Testing and Materials[35]), the accelerated ageing process of elastomeric and sliding bearings are based on exposure of specimens to high temperatures T_{ref} (typically in the range 60°–80°) in a vacuum for known (generally relatively short) periods of time t_{ref}. However, the age of the treated specimens represented in these laboratory tests is not specified, confirming that this approach can be useful in the comparison of various rubber compounds but is unsuitable for the prediction of life expectancy of the elastomeric bearings.[36] For just that purpose, in the present work, the Arrhenius methodology is adopted to correlate the accelerated ageing results with the ageing under service conditions[37,38]:

$$\ln\left(t_{ref}/t\right) = E_a/R_g \cdot \left(T_{ref}^{-1} - T^{-1}\right), \tag{13}$$

t being the real time; E_a(=9.04 × 10^4 J/mol) the activation energy of the rubber; R_g(=8.31 J/mol/K) the gaseous constant.

Curves representing variability of the mechanical properties with time of accelerated ageing (t_{ref}), at the controlled temperature T_{ref} = 80°C and service mean temperature T = 20°C, are plotted in Figure 1. Specifically, shear modulus of the HDRBs (i.e., $G(t)$ in Figure 1a), for three elastomer compounds (i.e., soft, S, normal, N, and hard, H) and static friction coefficient of the FSBs (i.e., $\mu_s(t)$ in Figure 1b), for low (L) and medium (M) friction, is represented starting from the nominal (unaged) value. As a comparison, an additional axis of abscissa is reported in order to represent the equivalent time of ageing obtained with the Arrhenius method. It is worth noting that heat ageing tests after an expected time of 17, 33, 50, and 67 days correspond to 25, 50, 75, and 100 years when T_{ref} = 80°C is considered but an unrealistically high value of the reference time should be considered for the prediction of the life expectancy when T_{ref} = 60°C or T_{ref} = 70°C is assumed. As expected, an increase of stiffness (Figure 1a) and friction threshold (Figure 1b) is observed for increasing values of t_{ref}.

2.2 | Time-dependent effects: Air temperature

Mechanical properties of the HDRBs can also change significantly due to weather conditions: that is, variations in the environmental temperature over long periods of time, such as wide variations in air temperature between winter (e.g., with a mean value of 10°C) and summer (e.g., with a mean value of 25°C). Specifically, experimental tests carried out on the HDRBs show that both the stress level and the area encompassed by the hysteresis loop increase more than linearly whereas air temperature is decreasing, especially when the temperature[7] drops below 0. Moreover, at a given temperature, these effects increase from soft-to-normal elastomer compounds and from normal-to-hard elastomer compounds.[10] Furthermore, undetectable sensitivity of the cyclic behaviour to the thermal history of the specimen is observed, whereas the equivalent viscous damping remains practically unchanged over the whole range of air temperature. The results also indicate that the lateral stiffness increases more than linear when the air temperature falls significantly compared with the mean working condition (i.e., T = 20°C); at the same time, rising temperatures do not lead to abrupt variations in lateral stiffness. On the basis of the experimental curves at 100% of shear strain,[10] the secant shear modulus variability with air temperature (T) can be expressed by the following polynomial laws, distinguishing soft (SC):

$$G_{SC}(T) = 0.508 - 9.779{\cdot}10^{-3}{\cdot}T + 3.603{\cdot}10^{-4}{\cdot}T^2 - 8.843{\cdot}10^{-6}{\cdot}T^3 + 8.967{\cdot}10^{-8}{\cdot}T^4\ [\text{MPa}], \tag{14}$$

normal (NC),

$$G_{NC}(T) = 1.039 - 1.468{\cdot}10^{-2}{\cdot}T + 4.204{\cdot}10^{-4}{\cdot}T^2 - 2.275{\cdot}10^{-5}{\cdot}T^3 + 4.29{\cdot}10^{-7}{\cdot}T^4\ [\text{MPa}], \tag{15}$$

and hard (HC)

$$G_{HC}(T) = 1.752 - 2.493{\cdot}10^{-2}{\cdot}T + 4.704{\cdot}10^{-4}{\cdot}T^2 - 7.452{\cdot}10^{-6}{\cdot}T^3 + 1.147{\cdot}10^{-7}{\cdot}T^4\ [\text{MPa}], \tag{16}$$

elastomer compounds. It should be noted that the selected compounds (i.e., SC, NC, and HC) present the nominal values of the shear modulus (i.e., 0.4, 0.8, and 1.4 MPa) provided by FIP (2014) when the selected temperature corresponds to the mean working temperature (i.e., T = 20°C). The corresponding axial moduli are evaluated through an expression similar to Equation (10).

$$E_{..}(T) = \left(\frac{1}{6 \cdot G_{..}(T) \cdot S_1^2} + \frac{4}{3 \cdot E_b}\right)^{-1} \tag{17}$$

Curves representing variability of mechanical properties of HDRBs with air temperature are plotted in Figure 2. Specifically, shear (Figure 2a) and axial (Figure 2b) moduli of the HDRBs for SC, NC, and HC elastomer compounds are represented in the range of temperatures from −20°C to 40°C. Vertical lines corresponding to winter and summer mean seasonal temperatures are also reported as threshold values considered in the numerical study. As can be observed, the rate of reduction of the axial modulus with temperature (Figure 2b) is less evident than that of observed for the shear modulus (Figure 2a) as a result of Equation (10) where $G_{..}(T)$ only concerns the first part of $E_{..}(T)$.

Finally, experimental results corresponding to different pressure–velocity couples of values highlight the fact that the dynamic friction coefficient decreases for increasing values of the air temperature.[13] Specifically, the rate of reduction is greater at low-to-medium temperature (i.e., −10°C to 20°C) than from medium-to-high (i.e., 20°C to 50°C) temperature, highlighting a decrease of about 2.5 times in the rate when the dynamic fast (μ_{fast}) instead of dynamic low (μ_{low}) friction coefficient is considered. Moreover, the dynamic friction coefficient is practically independent of the contact pressure. However, variation of the dynamic friction coefficient with temperature is significantly reduced in the range from 10°C to 25°C and therefore will not be considered in the present study.

2.3 | Seismic dependent effects

A simple but reasonably accurate model is required to describe the nonlinear hysteretic behaviour of the elastomeric bearings, given that axial forces significantly affect the horizontal response and softening in the vertical direction at large lateral deformations. Starting from experimental results,[15] the three-spring two-dashpot viscoelastic linear model shown in Figure 3a can be improved,[39] modifying the uncoupled elastic (F_{K0} and P_{K0}) and damping (F_{C0} and P_{C0}) axial forces, proportional to the horizontal and vertical displacement (u_H and u_V) and velocity ($\dot{u}_H$ and $\dot{u}_V$), respectively, and the spring moment (M_{K0}) proportional to the rotation (θ). In detail, nonlinear elastic springs in the horizontal and vertical directions can be considered and their coupling obtained with a modified vertical displacement (u_V^*) taking into account the axial shortening or lengthening due to second-order geometric effects. Moreover, the post-critical behaviour of an HDRB is unstable, so its response can be adequately predicted when the nonlinearities are fully accounted for.[18] Specifically, the horizontal and rotational stiffness lessens with increasing horizontal displacement, thereby requiring modified expressions of the nonlinear axial (horizontal) and rotational springs.

The following expressions can be used for the horizontal (i.e., F), vertical (i.e., P), and rotational (i.e., M) components of the refined model shown in Figure 3b:

$$F = F_{K1} + F_{C0} = K_{H1} \cdot u_H + C_{H0} \cdot \dot{u}_H \cong K_{H0} \cdot \left[1 - \left(\frac{P}{P'_{cr}}\right)^2\right] \cdot \left[1 - 0.325 \cdot \tanh\left(\alpha \frac{u_H}{t_r}\right)\right] \cdot u_H + \frac{\xi_H \cdot K_{H0} \cdot T_{1H}}{\pi} \cdot \dot{u}_H, \tag{18a}$$

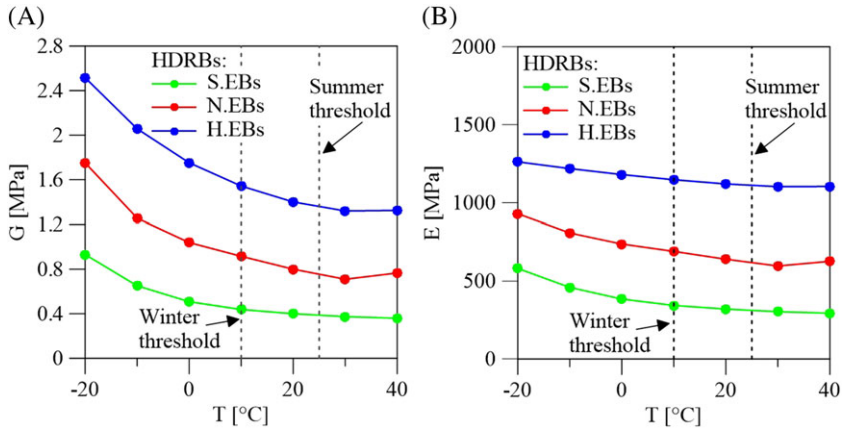

FIGURE 2 Effects of air temperature on the mechanical properties of the high-damping rubber bearings. (a) Shear modulus, (b) axial modulus

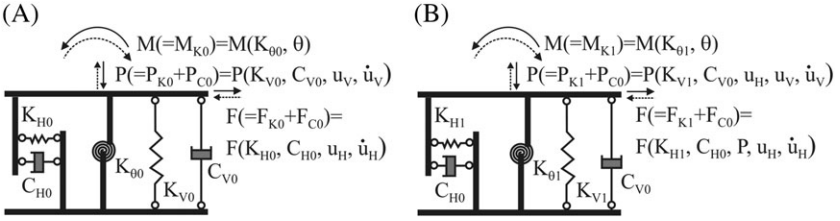

FIGURE 3 Effects of seismic loads on mechanical properties of the high-damping rubber bearings. (a) Simplified model, (b) refined model

$$P = P_{K1} + P_{C0} = K_{V1}\cdot u_V^{*} + C_{V0}\cdot \dot{u}_V \cong \frac{K_{V0}}{1+48\cdot\left(\frac{u_H}{\pi\cdot D}\right)^2}\operatorname{sgn}(u_V)\cdot\left(|u_V| - \frac{16\cdot\alpha_b}{\pi^2\cdot D\cdot S_2\cdot\alpha_{K0}}u_H^2\right) + \frac{\xi_V\cdot K_{V0}\cdot T_{1V}}{\pi}\cdot\dot{u}_V, \tag{18b}$$

$$M = M_{K1} = K_{\theta 1}\cdot\theta = K_{\theta 0}\cdot\left[1 - \frac{25.4 - t}{D}\left(\alpha\frac{u_H}{t_r}\right)\right]\cdot\vartheta, \tag{18c}$$

where K_{H0} and K_{V0} are the nominal values of the horizontal and vertical stiffness at the design displacements and zero axial load; $\alpha_{K0} = K_{V0}/K_{H0}$ is the nominal stiffness ratio; $K_{\theta 0}$ is the rotational stiffness at zero shear strain; ξ_H (ξ_V) and T_{1H} (T_{1V}) represent, respectively, the equivalent viscous damping ratio and the fundamental vibration period in the horizontal (vertical) direction; $\alpha_b = h_b/t_r$, h_b being the total height of the bearing; $S_2 = D/t_r$ is the secondary shape factor; α is a dimensionless constant with a value of t_r. It should be noted that u_H in Equation 18a18c is expressed in millimeter. A reduced critical buckling load can be also introduced, with a bilinear approximation of the area-reduction method, which takes into account the finite buckling capacity of a bearing at zero overlap area[17]:

$$P_{cr}^{'} = 0.2\cdot P_{cr} \text{ for } \frac{A_r}{A} \le 0.2,\ P_{cr}^{'} = P_{cr}\cdot\frac{A_r}{A} \text{ for } \frac{A_r}{A} > 0.2,\ P_{cr} = \frac{\pi\cdot G\cdot S_1\cdot S_2\cdot A}{2\sqrt{2}}, \tag{18d}$$

where A_r is the reduced area due to lateral displacement. Note that the effect of cavitation on tensile response is not considered in the present study.[40]

Similarly, for constant values of the axial load (i.e., P = W, W being the weight of the superstructure) and friction coefficient (i.e., μ equal to the dynamic fast value μ_{fast}), the force-displacement behaviour of an FSB in the horizontal direction is generally idealized as a simplified rigid-plastic law (Figure 4a). However, experimental studies confirm the complex nonlinear behaviour of the FSBs, highlighting the presence of numerous parameters affecting their friction coefficient at the sliding surface. In particular, the dynamic friction coefficient monotonically increases with the sliding velocity up to a constant value.[19] Moreover, the response of the FSBs shifts between sticking and sliding phases, at the breakaway and motion reversals, highlighting a static friction coefficient greater than the dynamic one.[23] Yet the instantaneous pressure (p) due to the axial load during seismic motion (N) also affects the friction coefficient of an FSB, with a reduction of μ_{fast} for increasing values of pressure, whereas the dependence of μ_{slow} on the axial pressure is minimal and $\mu_{\text{slow}} = 0.4\mu_{\text{fast}}$–$0.5\mu_{\text{fast}}$ is generally assumed.[13,22] On that basis, the frictional force at the sliding interface can be expressed as (Figure 4b) follows:

$$F = k_p\cdot\left[\mu_{\text{fast}} - (\mu_{\text{fast}} - \mu_{\text{slow}})\cdot e^{-\alpha_1\cdot|\dot{u}_H|} + (\mu_s - \mu_{\text{slow}})\cdot e^{-\alpha_2\cdot|\dot{u}_H|}\cdot\frac{|\operatorname{sgn}(\dot{u}_H) - \operatorname{sgn}(u_H)|}{2}\right]\cdot P, \tag{19a}$$

where μ_s is the static friction coefficient when velocity[41] is 0, with $\mu_s/\mu_{\text{fast}} \cong 2$, α_1(=0.015 s/mm) is a parameter regulating the increase in dynamic friction with velocity, α_2(=0.25 s/mm) is a parameter regulating the transition from the static to the dynamic friction regime and

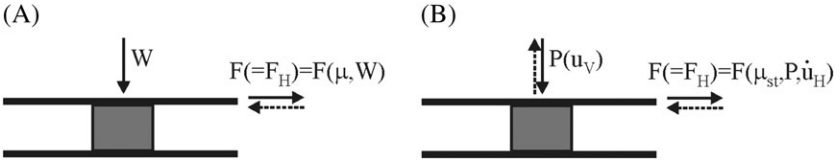

FIGURE 4 Effects of seismic loads on mechanical properties of the flat sliding bearings. (a) Simplified model, (b) refined model

$$k_p = 0.07^{0.02\cdot(p-p_o)}, \tag{19b}$$

represents the effect of the axial load (P), depending on vertical ($p_0 = P_0/A$) and seismic ($p = P/A$) pressure[22] on the sliding surface (A). Finally, it should be noted that variation of the friction coefficient with temperature at the sliding surface is not considered in the present study.

Furthermore, a gap element with infinitely rigid behaviour in compression is assumed in the vertical direction to consider the fact that an FSB does not resist tensile axial loads and is thus free to uplift

$$P = N \text{ for } u_V \geq 0 \text{ and } P = 0 \text{ for } u_V < 0. \tag{19c}$$

3 | BASE-ISOLATED STRUCTURAL SYSTEMS

Typical six-storey residential buildings with an r.c. framed structure isolated at the base by 20 identical HDRBs (i.e., elastomeric isolation system) or 14 HDRBs combined with six FSBs (i.e., hybrid isolation system) are considered for the numerical investigation (Figure 5). A double foundation system constituted of two grids of rigid beams is placed at the base of the framed structure, below, and above the isolation level. In view of the symmetric plan of the building, only the plane frames orientated along the horizontal ground motion direction (Y), perpendicular to the floor slab direction (X), are considered as reference.

The design vertical loads are divided in structural dead loads and live loads equal, respectively, to 3.5 and 2 kN/m^2 at all floors. Nonstructural dead loads are also applied, assuming: 1.67 kN/m^2, for the sixth floor, 3.47 kN/m^2, for the zero floor, and 3.07 kN/m^2, for the other floors. Finally, nonstructural masonry infills are taken into account through an additional dead load of 2.70 kN/m^2 along the perimeter. A cylindrical compressive strength of 25 N/mm^2 for the concrete and a yield strength of 450 N/mm^2 for the steel are assumed for the r.c. frame members. Horizontal and vertical seismic loads are evaluated in line with the current Italian code,[3] assuming high-risk seismic zone; elastic response of the superstructure (i.e., behaviour factors for the horizontal and vertical seismic loads, $q_H = q_V = 1.0$); medium subsoil type (i.e., subsoil class B); flat terrain (i.e., topographic class T1). Main parameters at the life-safety (LS) and collapse-prevention (CP) limit states, in the horizontal and vertical directions, are reported in Table 1: that is, peak ground

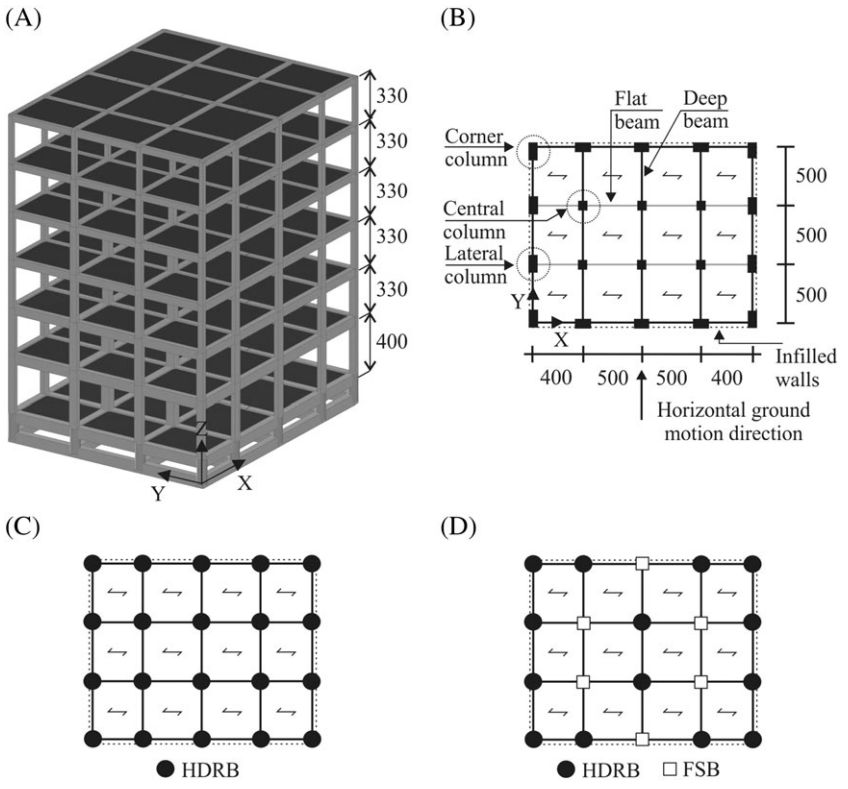

FIGURE 5 3D view and plans of the base-isolated structures (units in centimeter)

TABLE 1 Design parameters for horizontal (H) and vertical (V) seismic loads[3]

	PGA_H	PGA_V	S_H	S_V	F_H	F_V
LS limit state	0.260 g	0.181 g	1.147	1.000	2.428	1.677
CP limit state	0.349 g	0.281 g	1.056	1.000	2.466	1.711

Note. CP: collapse prevention; LS: life safety.

TABLE 2 Geometrical properties of the superstructure (units in centimeter and ton)

Storey	Corner column	Lateral column	Central column	Deep beam	Flat beam	m_i
6	30 × 30	30 × 30	30 × 30	30 × 45	40 × 25	2.600
5	30 × 35	30 × 40	40 × 40	30 × 45	40 × 25	2.846
4	30 × 40	30 × 50	50 × 50	30 × 50	50 × 25	2.989
3	30 × 40	30 × 50	50 × 50	30 × 55	50 × 25	3.123
2	30 × 50	30 × 60	60 × 60	40 × 60	60 × 25	3.458
1	30 × 50	30 × 60	60 × 60	40 × 70	60 × 25	3.671
0	-	-	-	50 × 100	50 × 100	4.418

acceleration (PGA_H and PGA_V); site amplification factor (S_H and S_V); maximum spectrum amplification coefficient (F_H and F_V). The fundamental vibration period of the base-isolated structures is assumed equal to 2.1 s in the horizontal direction, satisfying the condition $T_{BI} \geq 3T_{BF}$, T_{BF} being the value for the fixed-base structure. Moreover, the fundamental vibration period in the vertical direction is very low in case of the hybrid isolation system, although it depends on the vertical stiffness of the HDRBs for the elastomeric isolation system. The dimensions of the cross sections assumed for the beams (i.e., deep and flat) and columns (i.e., corner, lateral, and central) are reported in Table 2 where masses at the floor levels (i.e., m_i) are also presented. The design of the superstructure is carried out at the LS limit state so as to satisfy minimum conditions for the r.c. frame members in line with the provisions for low ductility class imposed by NTC18.[3]

3.1 | Elastomeric isolation systems

The elastomeric base-isolation (EBI) systems consist of three elastomer compounds for the 20 identical HDRBs and comply with the CP limit state, assuming a seismic design displacement equal to 28.9 cm and a nominal stiffness ratio $\alpha_{K0}(=K_{V0}/K_{H0})$ equal to 800. Specifically, soft (S.EBs, Figure 6a), normal (N.EBs, Figure 6b), and hard (H.EBs, Figure 6c) compounds are characterized by an unaged shear modulus (G_0) equal to 0.4, 0.8, and 1.4 MPa, respectively, and a volumetric compression modulus of the rubber (E_b) equal to 2,000 MPa. All three compounds ensure the same values of the equivalent viscous damping ratio for the EBI systems: that is, $\xi_H = 10\%$, in the horizontal direction; $\xi_V = 5\%$, in the vertical direction. Total shear strain $\gamma_{tot} \leq 5$ and shear strain due to seismic displacement $\gamma_s \leq 2$ are obtained. Moreover, the maximum compression axial load (P_{Ed}) does not exceed the critical load (P_{cr}) divided by a safety coefficient equal to 2.0, whereas the maximum tensile load does not exceed the ultimate value (P_{tu}). The latter is evaluated by

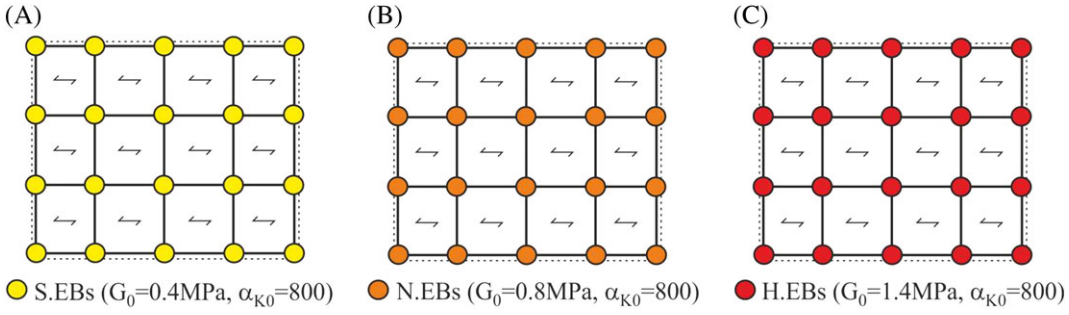

FIGURE 6 Elastomeric isolation systems with different elastomer compounds for the high-damping rubber bearings

TABLE 3 Geometrical properties of the high-damping rubber bearings (units in centimeter)

Compound	D_s	D_e	t_e	t_i	n_{si}	t_{si}	t_{se}	h
Soft (S)	68	68	14.1	1.3	11	0.21	3	22.1
Normal (N)	50	50	18.3	0.9	19	0.28	3	29.7
Hard (H)	46	46	22.4	0.5	45	0.40	3	45.9

TABLE 4 Design parameters of the high-damping rubber bearings at the collapse-perevention limit state (units in kN and centimeter)

Compound	γ_s	γ_{tot}	S_1	S_2	P_{cr}	P_{Ed}/P_{cr}	σ_s
Soft (S)	1.7	5	13	4.8	7573	0.30	18.2
Normal (N)	1.3	3.9	15.3	3.0	6474	0.35	17.6
Hard (H)	1.1	2.9	22.9	2.0	7216	0.31	12.5

multiplying the reduced effective area A_r (i.e., the area of overlap between the top and bottom of the isolator), which is a function of the lateral displacement,[42] and the ultimate tensile stress σ_{tu} (=min(2G, 1 MPa)) provided by the Italian code.[3] Finally, normal stress in the interior steel shims less than the yielding value (i.e., 235 MPa) is also satisfied. The following geometrical properties of the HDRBs are reported in Table 3: diameter of the steel layer (D_s) and that of the elastomer (D_e); total thickness (t_e) and thickness of the single layer (t_i) of elastomer; number (n_{si}) and thickness (t_{si}) of the interior steel shims; thickness of the exterior steel plates (t_{se}); and total height of the bearing (h). For each elastomer compound, the results of the verification are reported in Table 4.

As can be observed, for the same horizontal stiffness of the EBI system, the bearing diameter decreases for increasing values of the shear modulus whereas the opposite is the case for the bearing height. In order to comply with minimum values of the shape factors, the thickness of the elastomer layer decreases for increasing hardness of the elastomer compound. On the other hand, to limit normal stress of the interior steel shims, their thickness increases from soft-to-hard elastomer compound. It is interesting to note that for soft compound, the seismic design of the HDRBs depends on the condition imposed on the maximum values of γ_{tot}, whereas the control on the secondary shape factor S_2 proves to be the most conservative verification in the case of hard compound.

3.2 | Hybrid elastomeric-friction isolation systems

Six hybrid elastomeric-sliding base-isolation (ESBI) systems are designed at the CP limit state, given 14 identical HDRBs, with three elastomer compounds (i.e., S.EBs, N.EBs, and H.EBs), acting in parallel with six FSBs (four internally placed and two along the perimeter), and characterized by low-type (i.e., L.SBs in Figure 7a,c) and medium-type (i.e., M.SBs in Figure 7d,e) friction properties.

This arrangement corresponds to a value of 0.37 for the nominal sliding ratio $\alpha_{S0}(=F_{S0}/F_{S0,\max})$ of the FSBs under gravity loads, defined as the sliding force (F_{S0}) of the entire sliding system divided by the maximum sliding force ($F_{S0,\max}$) corresponding to a sliding bearing below each column of the test structure. The nominal stiffness ratio adopted for the ESBI systems is the same as the EBI ones (i.e., $\alpha_{K0} = 800$). The set of static (μ_s) and dynamic (μ_{slow} and μ_{fast}) friction parameters of the FSBs assumed in the analyses is reported in Table 5, where axial loads in the quasipermanent combination (P_{sd}) are also shown. For FSBs with medium-type friction, the coefficients are twice those for low-type friction.

Once a value equal to 10% is assumed for the equivalent viscous damping corresponding to the ESBI systems, where the weighted equivalent viscous damping ratios of the elastomeric ($\xi_{H,HDRBs}$) and sliding ($\xi_{H,FSBs}$) isolators are considered in line with the following expression.[43]

$$\xi_H = \frac{W_{h,HDRBs} + W_{h,FSBs}}{4\cdot\pi\cdot\left(W_{s,HDRBs} + W_{s,FSBs}\right)}100 = \xi_{H,HDRBs} + \xi_{H,FSBs}, \tag{20}$$

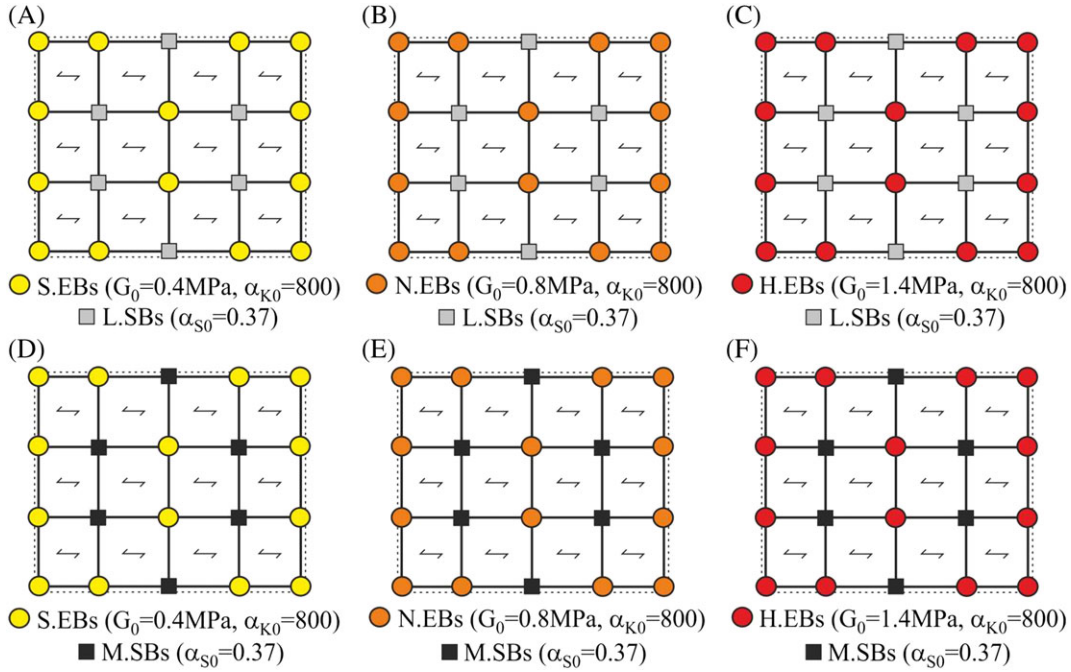

FIGURE 7 Hybrid elastomeric-sliding isolation systems with different elastomer compounds for the high-damping rubber bearings and friction threshold for the flat sliding bearings

TABLE 5 Mechanical properties of the flat sliding bearings (units in kN)

Friction type	μ_s	μ_{slow}	μ_{fast}	P_{Sd} (lateral)	P_{Sd} (central)
Low (L)	5%	1%	2.5%	905	1,243
Medium (M)	10%	2.5%	5%	905	1,243

$W_{s,HDRBs}$ and $W_{s,FSBs}$ being the strain energies at the secant stiffness corresponding to the design displacement (i.e., 28.9 cm), whereas $W_{h,HDRBs}$ and $W_{h,SBs}$ represent the hysteretic energies in a cycle of motion at the same displacement. Damping properties of the ESBI systems are shown in Table 6, assuming an equivalent viscous damping ratio of the HDRBs in the vertical direction of 5%.

Finally, Tables 7 and 8 summarize the geometrical properties and design parameters for HDRBs of the ESBI systems with reference to low-type friction of the FSBs, whereas analogous values are reported in Tables 9 and 10 in the case of medium-type friction. It is noteworthy that the design of the HDRBs is generally limited by the condition imposed on the maximum values of γ_s, whereas comparable geometric dimensions of the HDRBs are obtained by considering low- and medium-type friction properties of the FSBs.

4 | NUMERICAL RESULTS

A numerical study is carried out to investigate the effects produced by the variability of the mechanical properties of elastomeric (EBI systems) and hybrid elastomeric-sliding (ESBI systems) bearings due to ageing and air temperature. In order to reflect the increase of both stiffness of the HDRBs and static friction coefficient of the FSBs over their

TABLE 6 Damping properties of the hybrid isolation systems (units in kN and centimeter)

Friction type	$W_{h,HDRBs}$	$W_{s,HDRBs}$	$W_{h,FSBs}$	$W_{s,FSBs}$	$\xi_{H,HDRBs}$	$\xi_{H,FSBs}$	$\xi_{V,HDRBs}$	$\xi_{V,FSBs}$
Low (L)	88,992	83,960	19,593	2,449	8	2	5	-
Medium (M)	69,399	81,511	39,186	4,898	7	3	5	-

TABLE 7 Geometrical properties of the high-damping rubber bearings for the low-friction flat sliding bearings (units in centimeter)

Compound	D_s	D_e	t_e	t_i	n_s	t_{si}	t_{se}	h
Soft (S)	81	81	14.5	1.6	9	0.21	3	22.2
Normal (N)	61	61	16.3	1.0	16	0.28	3	26.5
Hard (H)	46	46	16.1	0.5	32	0.4	3	34.6

TABLE 8 Design parameters of the high-damping rubber bearings at the collapse-prevention limit state for the low-friction flat sliding bearings (units in kN and centimeter)

Compound	γ_s	γ_{tot}	S_1	S_2	P_{cr}	P_{Ed}/P_{cr}	σ_s
Soft (S)	2.0	4.4	13.0	5.6	12,608	0.15	12.3
Normal (N)	1.8	4.0	15.3	3.8	9,626	0.19	14.0
Hard (H)	1.8	4.0	22.9	2.9	8,484	0.22	14.2

TABLE 9 Geometrical properties of the high-damping rubber bearings for the medium-friction flat sliding bearings (units in centimeter)

Compound	D_s	D_e	t_e	t_i	n_s	t_{si}	t_{se}	h
Soft (S)	80	80	14.5	1.5	9	0.21	3	22.2
Normal (N)	61	61	16.8	1.0	17	0.28	3	27.2
Hard (H)	46	46	16.6	0.5	33	0.4	3	35.5

TABLE 10 Design parameters of the high-damping rubber bearings at the collapse-prevention limit state for the medium-friction flat sliding bearings (units in kN and centimeter)

Compound	γ_s	γ_{tot}	S_1	S_2	P_{cr}	P_{Ed}/P_{cr}	σ_s
Soft (S)	2.0	4.5	13.0	5.5	11,991	0.15	12.7
Normal (N)	1.7	3.9	15.3	3.6	9,626	0.19	14.0
Hard (H)	1.7	3.9	22.9	2.8	8,236	0.22	14.2

lifetime, different ageing times (i.e., $t_{ref} = 17$, 33, 50, and 67 days) are taken into account in the accelerated thermal oxidation test at reference temperature of $T_{ref} = 80°C$. Moreover, the sensitivity of the HDRBs to air temperature variations is evaluated by referring to mean seasonal (i.e., $T = 10°C$ in the winter and $T = 25°C$ in the summer) and annual (i.e., $T = 20°C$) values. For comparison, system properties modification factors proposed by the American code for new buildings[1] are also considered. Specifically, all the maximum or minimum λ factors for each event are multiplied together.[14]

$$\lambda_{\min} = \left[1 - f_a\left(\lambda_{ae,\min} - 1\right)\right] \cdot \lambda_{\text{test},\min} \cdot \lambda_{spec,\min}; \quad \lambda_{\max} = \left[1 - f_a\left(\lambda_{ae,\max} - 1\right)\right] \cdot \lambda_{\text{test},\max} \cdot \lambda_{spec,\max}, \tag{21ab}$$

where factors λ_{ae}, λ_{test}, and λ_{spec} encompass, respectively, ageing and environmental effects, variation observed during tests, and specification tolerances, whereas adjustment factor f_a provides for the reduced probability that several additive effects occur simultaneously. In the present work, different modification factors are applied to the HDRBs (i.e., $\lambda_{\min,\text{HDRBs}} = 1$ and $\lambda_{\max,\text{HDRBs}} = 1.225$) and FSBs (i.e., $\lambda_{\min,\text{FSBs}} = 1$ and $\lambda_{\max,\text{FSBs}} = 1.42$), on the assumption that $\lambda_{\text{test}} = \lambda_{\text{spec}} = 1.0$ and with reference to ordinary buildings (i.e., $f_a = 0.75$). A lumped plasticity model based on the Haar–Kàrmàn principle is used to describe the inelastic behaviour of r.c. frame members of the superstructure,[44] assuming a bilinear moment–curvature law with hardening ratio equal to 3%. Plastic conditions are checked at the potential critical sections of beams (i.e., end, quarter-span, and mid-span sections of the sub-elements in which a beam is discretized) and columns (i.e., end sections). With a view to studying the effects of advanced nonlinear modelling of the EBI and ESBI isolation systems, the formulations of the HDRBs and FSBs previously described in Section 2.3 are implemented through a computer code already proposed.[44] In the Rayleigh hypothesis, the damping matrix of the

superstructure is assumed as a linear combination of the mass and stiffness matrices, assuming horizontal and vertical viscous damping ratios (i.e., $\xi_{H,S}$ and $\xi_{V,S}$) equal to 2% with reference to the corresponding fundamental vibration periods (i.e., T_{1H} and T_{1V}). Nonlinear dynamic analyses of the EBI and ESBI structural systems, subjected to the horizontal and vertical components of near-fault earthquakes, are terminated once the ultimate state of the superstructure (in terms of curvature ductility of beams and columns) and ultimate shear deformations (i.e., $\gamma_{tot,u} = 1.5 \times 5 = 7.5$ and $\gamma_{s,u} = 1.5 \times 2 = 3$) and ultimate axial loads (i.e., P_{cr} and P_{tu}) of the HDRBs are attained.

4.1 | Fragility analysis for unscaled ground motions

The 20 near-fault ground motion records selected for this first part of the numerical investigation are selected from the Pacific Earthquake Engineering Research Center database[32] and are classified as pulse type in accordance with a pulse indicator.[45] Specifically, the two-sided (i.e., forward directivity) long-period horizontal velocity pulses are characterized by shear-wave velocity of the subsoil in the top 30 m, generally within the range corresponding to the subsoil type at the site in question (i.e., subsoil class B, 360 m/s $\leq V_{s,30} \leq$ 800 m/s). The Modified Acceleration Spectrum Intensity (MASI) measure is evaluated for both the horizontal components, integrating spectral values of acceleration in the range of vibration periods between a lower limit (i.e., $0.5 \times T_{BI} = 1.05$ s), accounting for the contribution of higher modes to structural response, and an upper limit (i.e., $1.25 \times T_{BI} = 2.63$ s), including the lengthening of vibration period due to the nonlinear structural behaviour.[46] This structure-specific integral seimic intensity measure can be considered efficient for predicting engineering demand parameters.[47] Note that only the horizontal component with the highest value of MASI is considered in the nonlinear dynamic analyses. In Table 11, the main data of the selected near-fault motions are shown: that is, earthquake location, date, recording station, magnitude (M_w), closest distance to the fault (Δ), peak ground acceleration (PGA_H), and $MASI_H$ of the selected horizontal component.

First, the nonlinear dynamic analysis of the EBI and ESBI structural systems subjected to the set of 20 unscaled ground motion histories is performed. For each record, the final instant of simulation is assumed as that corresponding

TABLE 11 Main data of the selected ground motions

Earthquake	Date	Station	M_w	Δ (km)	$V_{S,30}$ (m/s)	PGA_H (g)	$MASI_H$ (m/s)
Coyote Lake	06/08/1974	Gilroy Array #6	5.7	3.11	663.3	0.422	3.16
Tabas	16/09/1978	Tabas	7.4	2.05	766.8	0.854	8.29
Mammoth Lakes-06	27/05/1980	Long Valley Dam	5.9	16.03	537.2	0.414	2.80
Superstition Hills	24/11/1987	Parachute Test Site	6.5	0.95	348.7	0.432	12.89
Loma Prieta	18/10/1989	Gilroy–Gavilan Coll.	6.9	9.96	729.7	0.359	6.71
Erzincan	13/03/1992	Erzincan	6.7	4.38	352.1	0.496	5.70
Cape Mendocino	25/04/1992	Petrolia	7.0	8.18	422.2	0.591	5.19
Landers	28/06/1992	Barstow	7.3	34.86	370.1	0.135	3.04
Northridge	17/01/1994	Rinaldi Receiving Station	6.7	6.50	282.3	0.874	12.01
Kobe	16/01/1995	Takatori	6.9	1.47	256.0	0.618	18.27
Kocaeli	17/08/1999	Arcelik	7.5	13.49	523.0	0.134	5.53
Chi-Chi	20/09/1999	TCU068	7.6	0.32	487.3	0.512	10.68
Chi-Chi	20/09/1999	TCU076	7.6	2.70	615.0	0.428	1.42
Chi-Chi	20/09/1999	TCU079	7.6	10.70	364.0	0.592	5.76
Chi-Chi	20/09/1999	TCU102	7.6	1.49	714.3	0.304	8.27
Parkfield	28/09/2004	Cholame 2E	6.0	4.08	522.7	0.477	1.15
Parkfield	28/09/2004	Cholame 3E	6.0	5.55	397.4	0.800	0.83
Parkfield	28/09/2004	Cholame 4W	6.0	4.23	410.4	0.575	1.39
Chuetsu-oki	16/07/2007	Oguni Nagaoka	6.8	20.0	561.6	0.625	2.64
L'Aquila	06/04/2009	V. Aterno–Centro Valle	6.3	6.27	475.0	0.664	4.24

to the attainment of an ultimate condition of r.c. frame members of the superstructure and/or HDRBs of the base-isolation system in the conventional design configuration (i.e., $t = 0$ days and $T = 20$°C). Afterwards, in order to make the results comparable, the analyses are repeated assuming this value as the final instant of simulation for each ground motion and base-isolated system. The cloud method is adopted for the fragility analysis,[31] based on fitting a linear regression model in the logarithmic scale to the pairs of an engineering demand parameter (EDP), representative of the structural response, versus an intensity measure for a suite of unscaled ground motions. In Figures 8 and 9 are reported cloud data of the EBI and ESBI structures, respectively, obtained by combining a scalar demand to capacity ratio of the EDP, that is equal to unity at the onset of the ultimate limit state, with an intensity measure.[48]

In particular, maximum values of ductility demand at the end sections of the beams (Figures 8a–c and 9a–c) and total shear strain of the HDRBs (Figures 8d–f and 9d–f) are plotted against the MASI values corresponding to the elastic response spectra of acceleration of the interrupted records. Plots refer to three elastomer compounds of the HDRBs (i.e., the EBI.S, EBI.N, and EBI.H structures), which may be combined with low friction of the FSBs (i.e., the ESBI.SL, ESBI.NL, and ESBI.HL structures). The dependence of mechanical properties of the HDRBs on air temperature variations is taken into account by considering winter ($T = 10$°C) and summer ($T = 25$°C) mean values of temperature, in the aged state corresponding to $t_{ref} = 33$ days and $T_{ref} = 80$°C. Results for the lower-bound (λ_{min}) and upper-bound (λ_{max}) limit values of the ASCE modification factor are also presented for comparison. As can be observed, the significant dispersion in the MASI values of the selected ground motions and the occurrence of a number of demand to capacity EDP ratios greater than unity lead to reasonable fragility estimates. Specifically, the maximum ductility demand of beams at the lower storeys of the test structures is always responsible for the conventional structural failure at $t = 0$ days and $T = 20$°C (i.e., λ_{min}). The decrease in temperature leads to an increase of the ductility demand (see blue points in Figures 8a–c and 9a–c), whereas the opposite happens for the total shear strain when air temperature rises (see red points in Figures 8d–f and 9d–f).

In order to estimate the probability that a given level of damage will occur in the EBI and ESBI structures, undergoing a given ageing time at different air temperatures, fragility analysis needs to be developed. To this end, a robust fragility software based on the cloud data above described is adopted for an efficient fragility assessment.[48] Fragility curves of the EBI and ESBI structures are reported in Figures 10 and 11, respectively, with reference to the

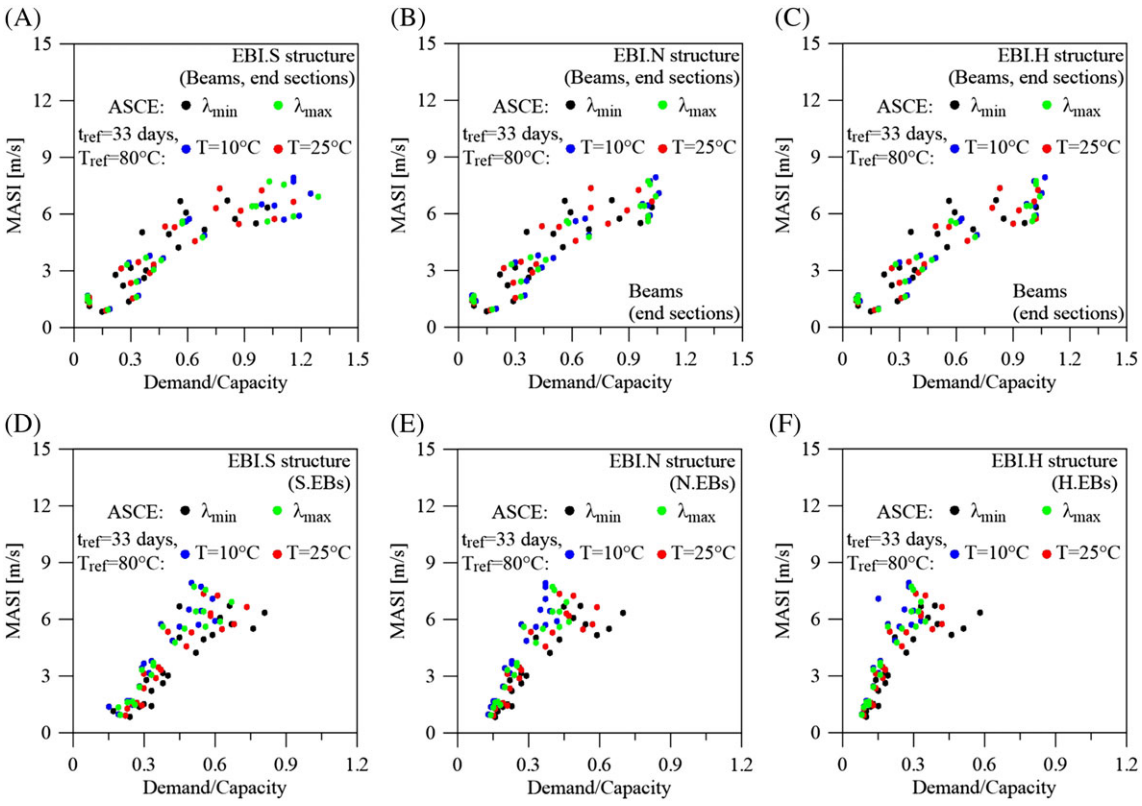

FIGURE 8 Cloud data of the structural systems with elastomeric base-isolation system: (a–c) ductility demand of beams; (d–f) total shear strain of high-damping rubber bearings

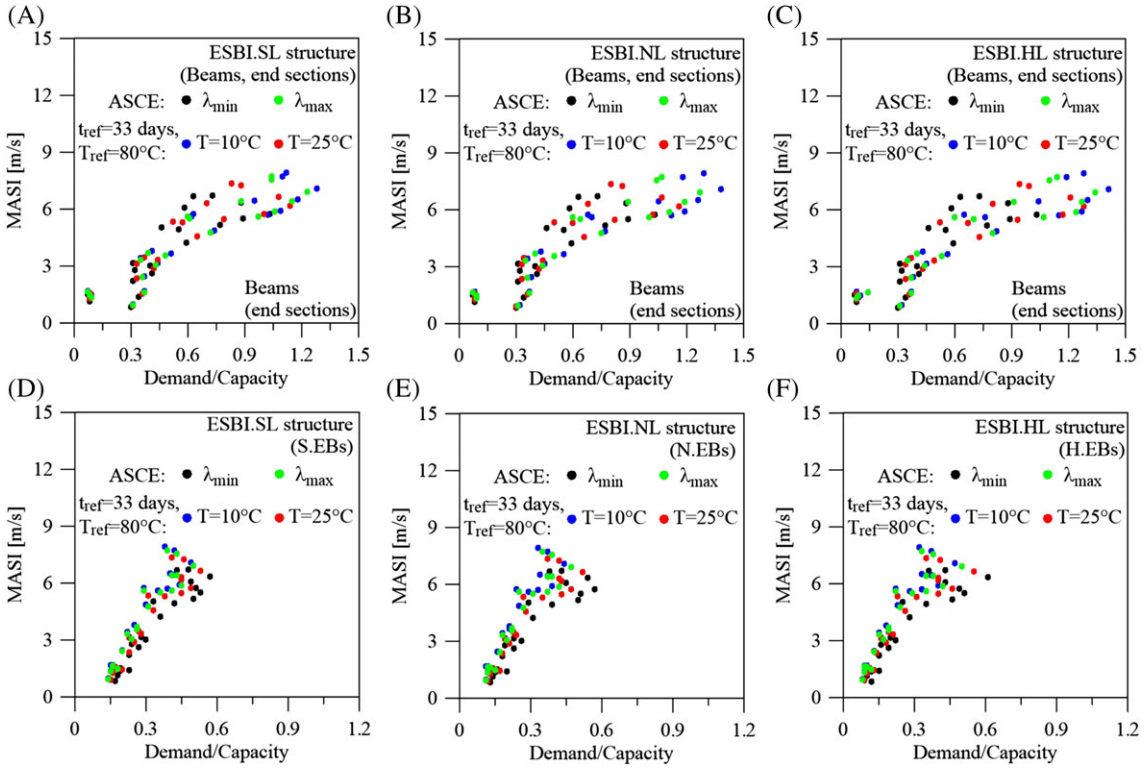

FIGURE 9 Cloud data of the structural systems with hybrid elastomeric-friction base-isolation system: (a–c) ductility demand of beams; (d–f) total shear strain of high-damping rubber bearings

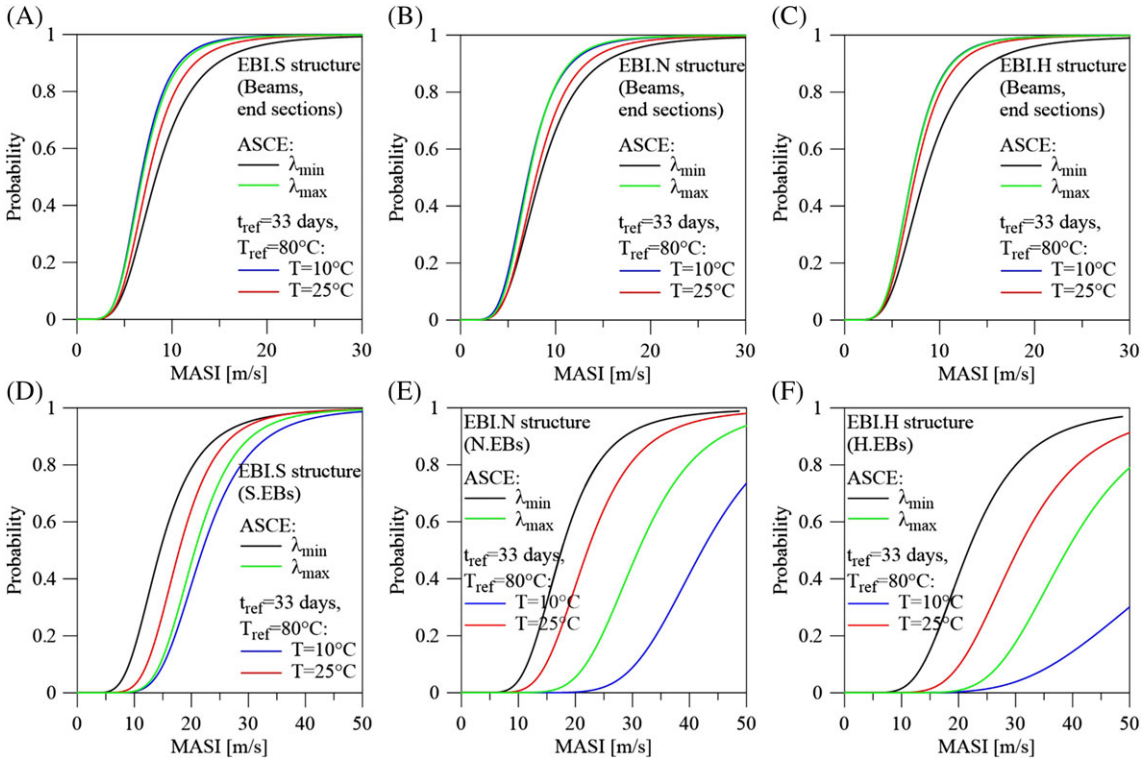

FIGURE 10 Fragility curves of the structural systems with elastomeric base-isolation system: (a–c) ductility demand of beams; (d–f) total shear strain of high-damping rubber bearings

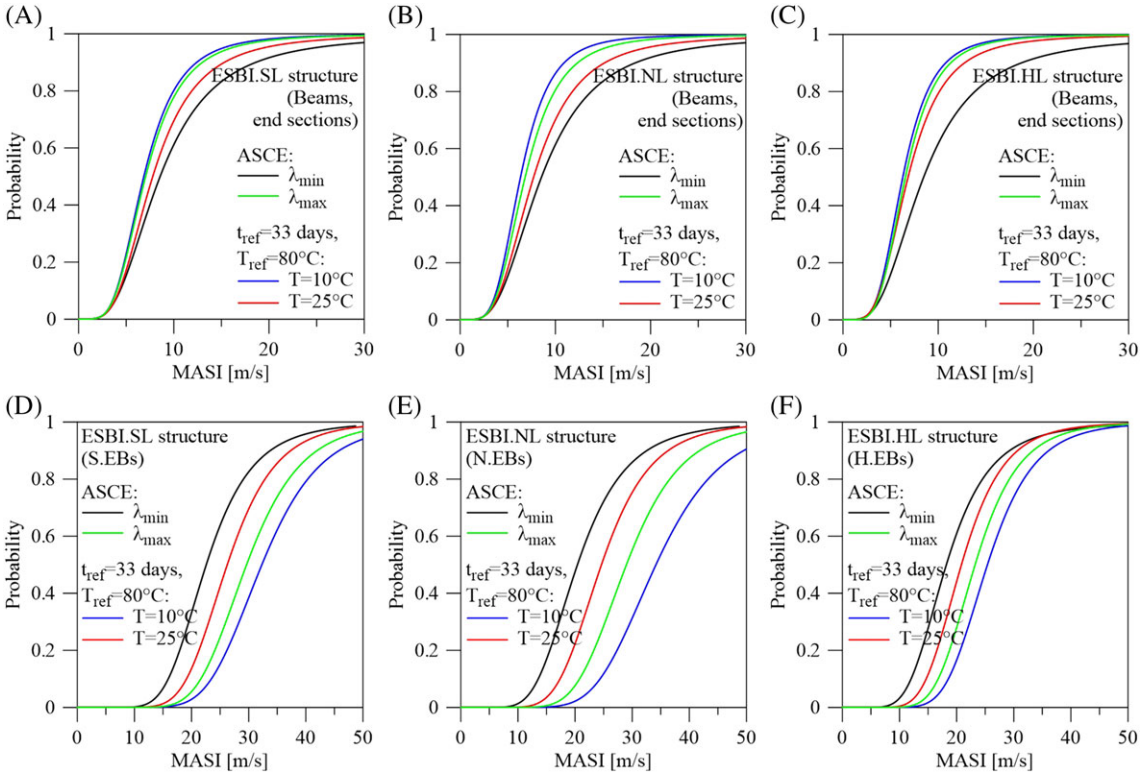

FIGURE 11 Fragility curves of the structural systems with hybrid elastomeric-friction base-isolation system: (a–c) ductility demand of beams; (d–f) total shear strain of high-damping rubber bearings

superstructure and base-isolation system. Namely, the fragility curves plotted in Figures 10a–c and 11a–c provide information about the probability of exceeding a particular state of damage of the superstructure conditioned on ductility demand, whereas total shear strain-based fragility functions return a similar result for the base-isolation system (Figures 10d–f and 11d–f).

It is noted that fragility curves referring to the minimum (λ_{min}) and maximum (λ_{max}) values of ASCE modification factors almost always envelope curves, which are the effects of the long-term behaviour of the superstructure (i.e., blue and red lines in Figures 10a–c and 11a–c), unlike base-isolation systems of the EBI (Figure 10d–f) and ESBI (Figure 11 d–f) structures whose fragility curves for $T = 10°C$ exceed those related to λ_{min}. Furthermore, the selection of different elastomer compounds produces a significant variability of fragility curves of the HDRBs whereas less pronounced effects are observed for the superstructure.

4.2 | Nonlinear dynamic analysis for scaled ground motions

A subset of seven near-fault earthquakes is selected from the Pacific Earthquake Engineering Research Center database,[32] already included in the set of 20 unscaled ground motions reported in Table 11. Specifically, the In-Spector software is adopted for a computer-aided selection of seven spectrum-compatible records, considering ground motions whose horizontal and vertical spectra match the design spectra proposed by Italian seismic code[3] at the CP limit state referring to a certain value of the root-mean-square difference between a real spectrum and the target spectrum.[49] Then, the selected earthquakes are scaled on the basis of design hypotheses for the test structures, assuming Italian geographical coordinates (i.e., longitude 39.3330° and latitude 16.1852°) at the site in question (i.e., subsoil class B). Distinct scale factors of the horizontal (SF_H) and vertical (SF_V) accelerograms are evaluated on the basis of MASI values. Mean spectra of the horizontal and vertical real motions, omitted for the sake of brevity, satisfy lower and upper bound tolerances of 10% and 30%, respectively, from the target design response spectra provided by NTC 2018 at the CP limit state. This assumption is similar to that provided by ASCE code, requiring that ground motions to be scaled up to the Maximum Considered Earthquake (MCE) level for analysis of base-isolated systems. In Table 12, the main data of the selected

earthquakes are reported: that is, earthquake location, date, recording station, peak ground accelerations (i.e., PGA_H and PGA_V), and scale factors (i.e., SF_H and SF_V) in the horizontal and vertical directions. The results discussed below are obtained as the mean of those obtained for each pair of records.

First, ductility demand of the beams along the building height is plotted in Figure 12, referring to the end (Figure 12 a–c), quarter-span (Figure 12d–f), and mid-span (Figure 12g–i) sections of the EBI. N structure characterized by normal elastomer compound of the HDRBs.

Ageing effects of the EBI systems are investigated assuming different test times (i.e., $t_{ref} = 17$, 33, 50, and 67 days at $T_{ref} = 80°C$) and three temperatures, representative of the winter ($T = 10°C$ in Figure 12a, 12d, and 12g), annual ($T = 20°C$ in Figure 12b, 12e, and 12h), and summer ($T = 25°C$ in Figure 12c, 12f, and 12i) mean values. It should be noted that λ_{min} curves correspond to the unaged design condition (i.e., $t_{ref} = 0$ days and $T = 20°C$) in Figure 12b, 12e, and 12g. As shown, the ductility demand increases due to the deterioration of the elastomeric isolation system that occurs for increasing values of ageing, with the highest rate in the end (Figure 12a–c) and quarter-span (Figure 12d–f) sections, which are sensitive to the horizontal seismic loads, unlike the mid-span sections (Figure 12g–i) mainly subjected to the vertical seismic loads. This can be explained by observing that over time, the increase of horizontal stiffness of the HDRBs, responsible for the reduction of the fundamental vibration period, is faster than the vertical stiffness.

Curves similar to the previous ones are reported in Figure 13, where the effects of different temperatures (i.e., $T = 10°C$, 20°C, and 25°C) are evaluated with reference to the unaged ($t = 0$ days in Figure 13a, 13d, and 13g) and aged ($t = 33$ and 67 days in Figure 13b, 13e, and 13h and 13c, 13f, and 13i, respectively) conditions.

As can be observed, the ductility demand of beams is notably affected by the air temperature, with increased values when winter cooling is considered. On the other hand, higher temperatures such as those corresponding to the summer heating partly compensate for ageing effects. The property modification factor approach appears, in many cases, representative of the deterioration phenomena of the isolation system; however, it is not conservative in the winter condition when the end of the nominal life of the structure is considered. Further results, omitted for the sake of brevity, confirm low values of the ductility demand in the columns of the superstructure, where deterioration of the HDRBs produces negligible variations.

Afterwards, to evaluate the effects of different choices for elastomer compound of the HDRBs, the distribution of the ductility demand is plotted in Figure 14, assuming the reference values of time (i.e., $t_{ref} = 33$ days) and temperature (i.e., $T_{ref} = 80°C$), which correspond to a nominal life of 50 years when the Arrhenius method is applied. The highest values of ductility demand are generally those corresponding to the hard elastomer compound, for the same horizontal stiffness of the HDRBs, whereas the soft compound prevails on the normal one when higher air temperature is considered (Figure 14d–f). In particular, two opposite effects combine because the ageing time is more pronounced in the case of the hard compound, characterized by the lowest diameter of the isolator, whereas the increase in temperature corresponds to a reduction of the shear modulus of rubber, which is higher for soft than for normal elastomer compound. Moreover, it is worth noting that the upper bound curve of the ASCE procedure (i.e., λ_{max}) is not found on the safety side for $T = 10°C$ (Figure 14a–c), given the fact that the variability with the elastomer compound has not been taken into account.

On the other hand, main parameters of the EBI system for the EBI.N structure are plotted in Figure 15, where different ageing (i.e., $t_{ref} = 17$, 33, 50, and 67 days at $T_{ref} = 80°C$) and temperature (i.e., $T = 10°C$, 20°C, and 25°C) conditions are combined. As can be observed, the process of ageing plays a favourable role on the response of the HDRBs, leading to a reduction of seismic (i.e., γ_s in Figure 15a) and total (i.e., γ_{tot} in Figure 15b) shear strains and an increase

TABLE 12 Main data of the selected ground motions at the collapse-prevention limit state

Earthquake	Date	Station	PGA_H (g)	PGA_V (g)	SF_H	SF_V
Tabas	16/09/1978	Tabas	0.854	0.641	0.50	0.40
Superstition Hills	24/11/1987	Parachute Test Site	0.432	0.000	0.40	0.00
Erzincan	13/03/1992	Erzincan	0.496	0.235	0.45	1.92
Cape Mendocino	25/04/1992	Petrolia	0.591	0.165	0.67	2.45
Kobe	16/01/1995	Takatori	0.618	0.284	0.35	1.07
Chi-Chi	20/09/1999	TCU068	0.512	0.530	0.40	0.93
Northridge	17/01/1994	Rinaldi Receiving Station	0.874	0.958	0.50	0.32

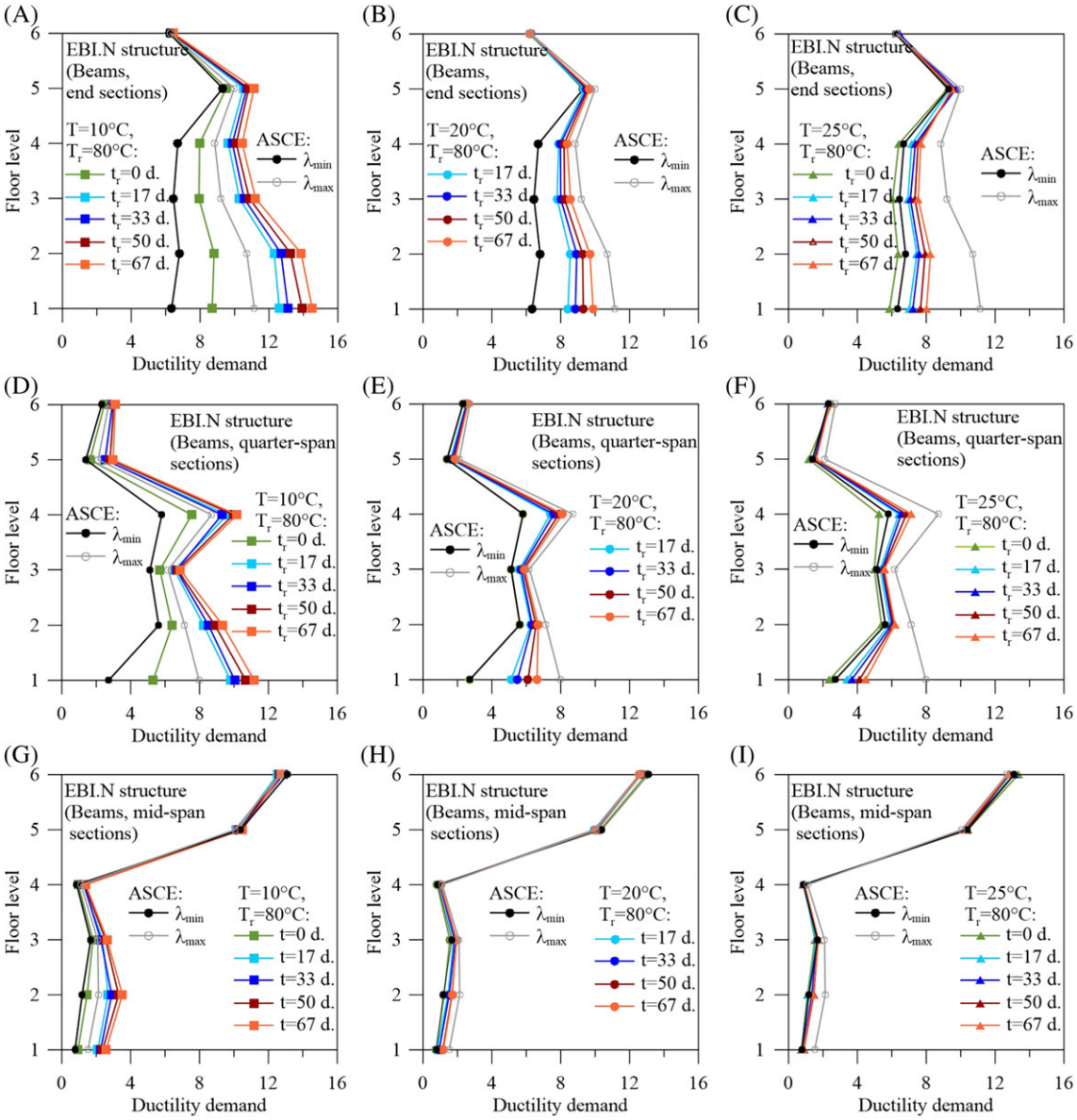

FIGURE 12 Effects of ageing on the elastomeric base-isolation systems at different temperatures on the ductility demand of the superstructure

of the critical buckling load (i.e., P_{cr} in Figure 15c). Moreover, the increase in temperature produces only a slight increase of the aforementioned strain parameters and a reduction of the buckling load ratio. It is should be noted that the NTC18 thresholds for the shear strains are largely satisfied (Figure 15a,b), whereas the NTC18 buckling threshold is borderline when the highest temperature (i.e., 25°C) is considered (Figure 15c). Finally, the lower-bound histogram of the ASCE procedure (i.e., $\lambda_{\min}$) is found to be the most favourable, enveloping in all the examined cases the effects of long-term behaviour of the isolation devices and exceeding the NTC18 buckling threshold in the cases of mean values of annual and summer temperature (Figure 15c).

Histograms similar to the previous ones are reported in Figure 16 to highlight the relationship between different types of rubber compound and variation of the material properties of the HDRBs over time and seasonal fluctuations in air temperature. The sensitivity in the hardness variation of the rubber is clearly shown by the seismic (i.e., γ_s in Figure 16a) and total (i.e., γ_{tot} in Figure 16b) shear strains, with maximum values during the lifetime of the base-isolation system corresponding to soft elastomer compound (green bar). The reason behind this response can be found in the seismic design of HDRBs leading to a reduction of the diameter and simultaneous increase of height passing from a soft to hard elastomer compound (see Table 3). Limited changes are observed with reference to the buckling load ratio

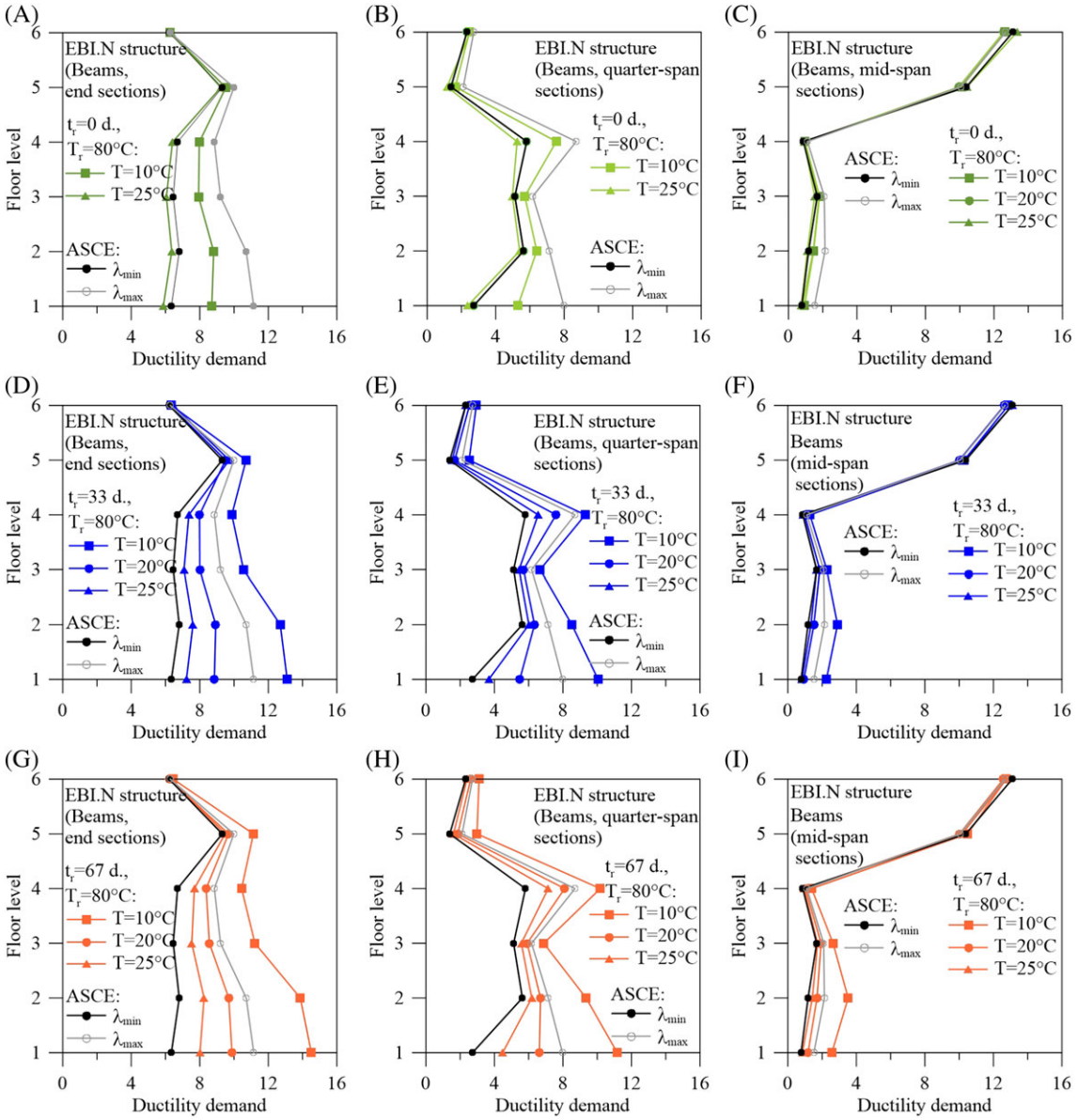

FIGURE 13 Effects of temperature on the elastomeric base-isolation systems at different ageing times on the ductility demand of the superstructure

(Figure 16c), highlighting a slight predominance of the normal elastomer compound affected by the highest value of the design value of this ratio (see Table 4).

In order to draw attention to the influence of the hybrid elastomeric-sliding base-isolation system on the nonlinear seismic response of the superstructure, local ductility demand of the beams is shown in Figure 17 referring to the ESBI. NL structure characterized by normal elastomer compound of the HDRBs combined with low-type friction of the FSBs. In particular, the effects of different air temperatures, at the reference time of 33 days, are compared with property modification factors made by applying the ASCE approach to elastomeric and sliding bearings. At the lower storeys, ductility demands at the end (Figure 17a) and quarter-span (Figure 17b) sections are inferior to those obtained for the corresponding structural systems with HDRBs acting alone (see Figure 13d,e). This means that the activation of the elastomeric bearings is delayed with the addition of the FSBs, depending on their friction threshold, and hence the variability of mechanical properties. On the contrary, the ductility demand increases at the mid-span sections of the upper storeys because of the greater vertical stiffness of the ESBI.NL structure (Figure 17c), but only limited variations may be seen similarly to the EBI. N structure (Figure 13f). Analogous results, omitted for the sake of brevity, are also found when changes in the ageing time are considered.

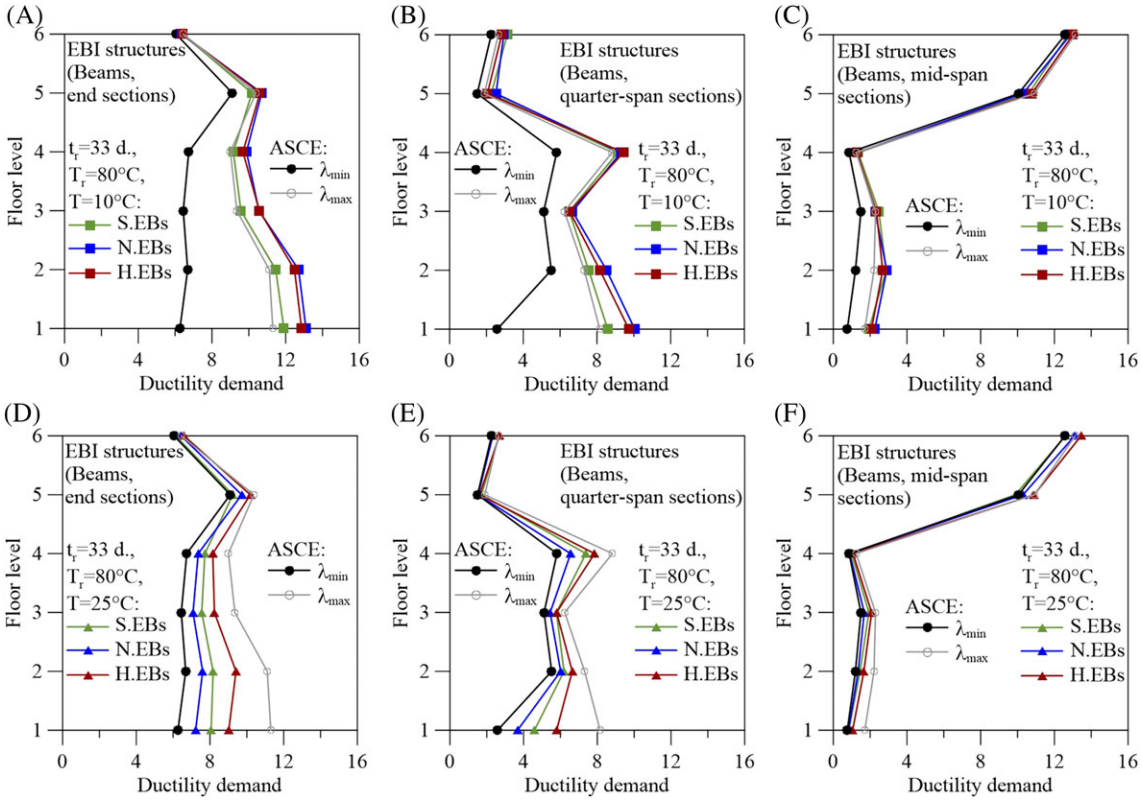

FIGURE 14 Effects of the elastomer compound of the elastomeric base-isolation systems on the ductility demand of the superstructure for different ageing times and temperatures

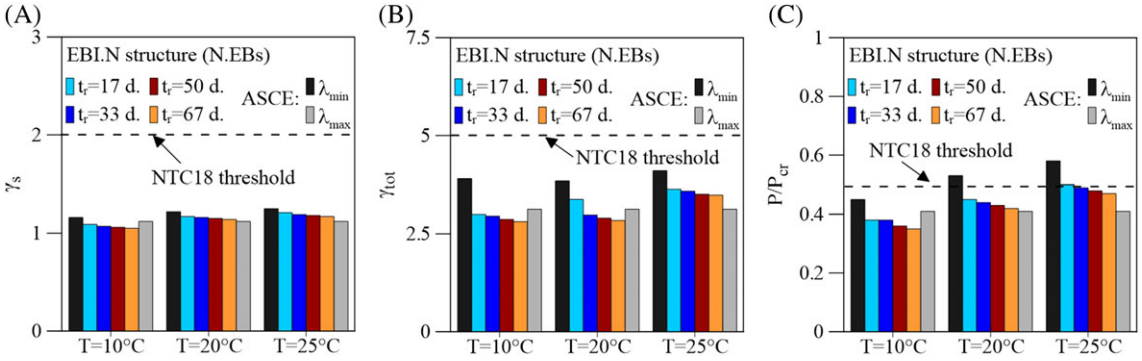

FIGURE 15 Main parameters of the elastomeric base-isolation systems with normal compound for different ageing times and temperatures of the high-damping rubber bearings

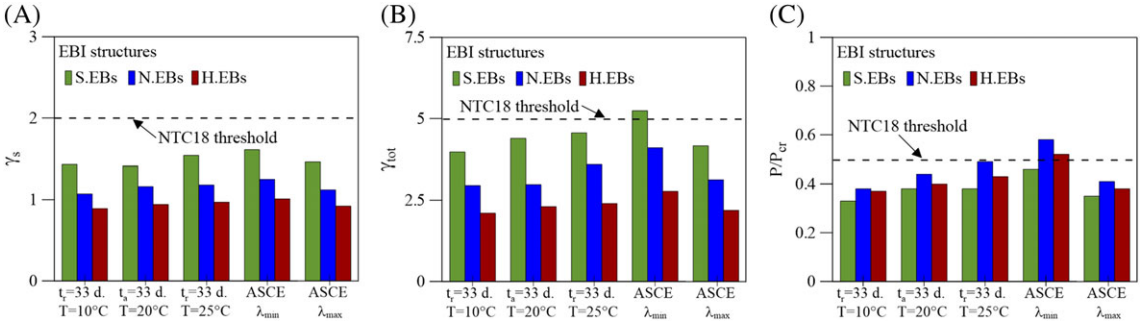

FIGURE 16 Main response parameters of the elastomeric base-isolation systems with assigned ageing times and temperatures, for different elastomer compounds of the high-damping rubber bearings

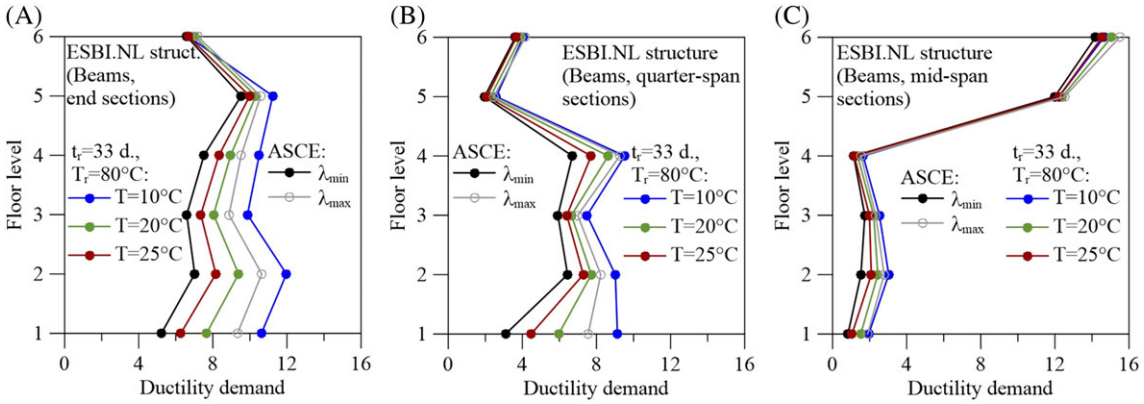

FIGURE 17 Temperature and ageing effects of the hybrid elastomeric-sliding base-isolation systems on the ductility demand of the superstructure

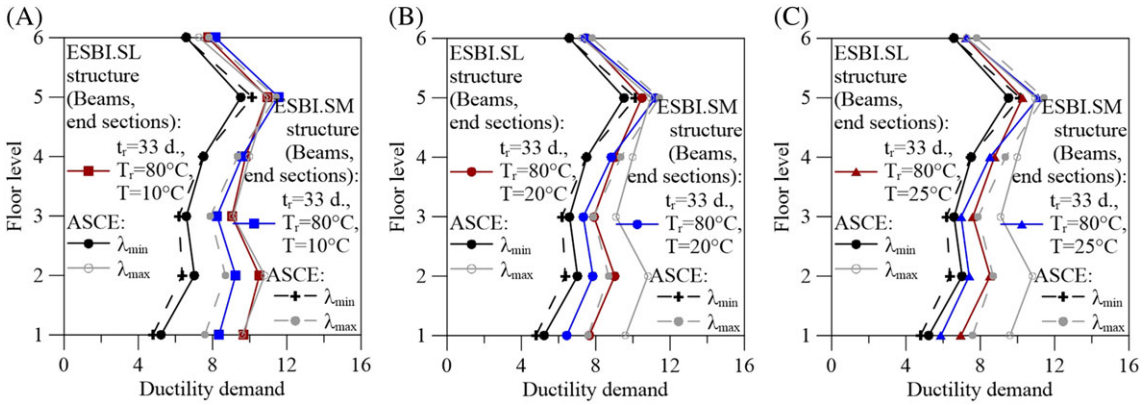

FIGURE 18 Friction effects of the flat sliding bearings on the ductility demand of the superstructure, assuming constant ageing time and variable temperature

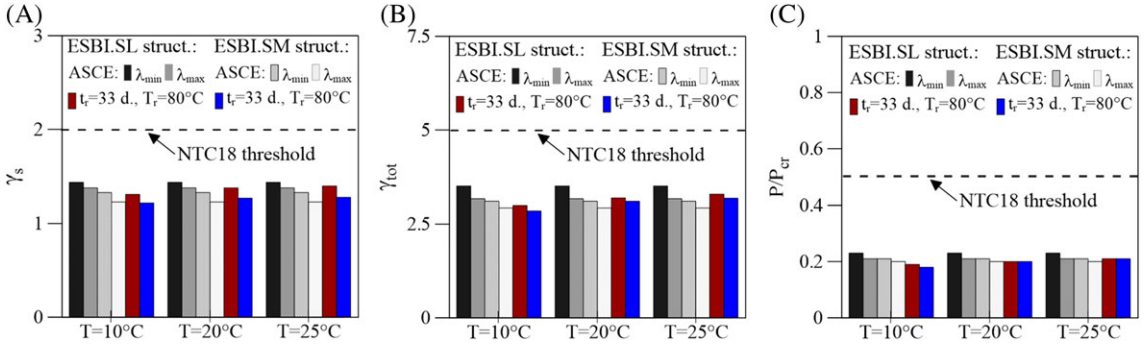

FIGURE 19 Friction effects of the flat sliding bearings on main response parameters of the high-damping rubber bearings, assuming constant ageing time and variable temperature

Finally, to investigate the influence of low (i.e., ESBI.SL structure) and medium (i.e., ESBI.SM structure) friction of the FSBs, combined with soft elastomer compound of the HDRBs, on the nonlinear seismic response of both superstructure (Figure 18) and base-isolation system (Figure 19). As before, the comparison will cover the condition corresponding to the nominal life (i.e., 33 days at 80°C, approximately equivalent to 50 years) and three different temperatures. It is worth noting that ductility demand at the end sections of beams is almost always greater for the ESBI.SL structure than

for the ESBI.SM. Here, again, the winter condition (i.e., $T = 10°C$) is confirmed as the heaviest for r.c. frame members (Figure 18a), and it is well reproduced by applying the property modification factors proposed by ASCE. Similarly, the HDRBs receive a beneficial effect from the presence of FSBs with medium-type friction coefficient rather than low-type friction coefficient (Figure 19). Note that changes in the main response parameters of the HDRBs cannot be attributed to the geometric properties of the HDRBs, these being almost identical (see Tables 7 and 9) but only to variations in the base-isolation response depending on the different friction properties of the FSBs.

5 | CONCLUSIONS

With the aim of quantifying the effects of mechanical property variability in elastomeric and sliding bearings on the nonlinear seismic response of base-isolated r.c. framed structures, a numerical model is proposed based on experimental results available in literature. Specifically, the influence of ageing and air temperature on the horizontal and vertical stiffnesses of the HDRBs and friction coefficient of the FSBs are investigated, although the equivalent viscous damping ratio of the HDRBs was found non-sensitive to these effects. First, nine structural solutions for the base-isolation system of six-storey r.c. framed structures are designed assuming nominal values of mechanical properties and considering two alternative arrangements: (a) EBI systems, with three different elastomer compounds for the HDRBs (soft, normal, and hard); (b) hybrid ESBI systems, with the aforementioned elastomer compounds of the HDRBs and two friction coefficients (low and medium) of the FSBs. A computer code including advanced nonlinear force-displacement laws of the isolation devices is implemented, also reflecting their long-term behaviour. Finally, fragility analysis of the test structures subjected to the horizontal components of unscaled earthquakes is carried out together with nonlinear dynamic analysis under the horizontal and vertical components of earthquakes scaled at the ultimate limit state. The results for the lower and upper bound property modification factors proposed by ASCE provide a comparison. The following conclusions can be drawn from the results presented in this study.

- Curves representing effects of accelerated ageing confirm that an increase of the horizontal stiffness of the HDRBs, and to a lesser extent vertical stiffness, and static friction coefficient of the FSBs is obtained for increasing values of the reference time.
- The equivalent time of ageing obtained with the Arrhenius method highlights that 25, 50, 75, and 100 years correspond to 17, 33, 50, and 67 days, respectively, when accelerated heat ageing tests at $T_{ref} = 80°C$ are considered, but an unrealistically high value of t_{ref} should be assumed for the prediction of life expectancy when $T_{ref} = 60°C$ or $T_{ref} = 70°C$ is assumed.
- Variability of shear and axial moduli of the HDRBs is observed for mean seasonal and annual temperatures, with an increase moving from summer to winter values. However, variation of the dynamic friction coefficient of the FSBs with temperature can be neglected.
- Fragility curves referring to the minimum (λ_{min}) and maximum (λ_{max}) ASCE values almost always envelope curves representing effects of the long-term behaviour of the superstructure, unlike for the base-isolation systems of the EBI and ESBI structures whose fragility curves for $T = 10°C$ exceed those related to λ_{min}.
- The selection of different elastomer compounds produces a significant variability of fragility curves of the HDRBs whereas less pronounced effects are observed for the superstructure.
- The ductility demand of the beams increases for increasing values of the ageing time of the elastomeric isolation system, with the highest rate at the end and quarter-span sections.
- The ductility demand of beams is notably affected by the air temperature, with increased values when winter cooling is considered. The property modification factor approach seems in many cases to be representative of the deterioration phenomena of the isolation system; however, it is not conservative in the winter condition when the end of the nominal life of the structure is considered.
- For the same horizontal stiffness of the HDRBs, the highest values of ductility demand are generally those corresponding to hard elastomer compound, whereas the soft elastomer compound prevails on the normal one when a higher temperature is considered. Moreover, the upper bound curve (i.e., λ_{max}) is not found on the safety side for $T = 10°C$ because the variability with the elastomer compound is not taken into account.
- The process of ageing plays a beneficial role on the response of the HDRBs, leading to a reduction of seismic and total shear strains and an increase of the critical buckling load, although only a slight worsening of the response

occurs when an increase in temperature is considered. The lower-bound histogram (i.e., λ_{min}) is conservative, enveloping in all the examined cases the effects of long-term behaviour of the isolation devices.
- Sensitivity to variation in hardness of the rubber is clearly shown by the seismic and total shear strains of the HDRBs, with maximum values corresponding to soft compound. Limited changes are observed with reference to the buckling load ratio.
- The activation of the HDRBs is delayed with the addition of the FSBs, depending on their friction threshold, and hence the impact in the variability of mechanical properties.
- The ductility demand at the end sections of beams is almost always greater for the ESBI.SL structure than for the ESBI.SM. Similarly, the HDRBs receive a beneficial effect from the presence of FSBs with medium-type friction coefficient rather than low-type friction coefficient.

ACKNOWLEDGEMENTS

The present work was financed by Re.L.U.I.S. (Italian network of university laboratories of earthquake engineering), in accordance with the "Convenzione D.P.C.–Re.L.U.I.S. 2019-2021, WPI, Isolation and Dissipation".

ORCID

Fabio Mazza https://orcid.org/0000-0003-1019-1333

REFERENCES

1. American Society of Civil Engineers. Minimum design loads for buildings and other structures, ASCE/SEI . 2017; 7–16.
2. Eurocode 8. Design of structures for earthquake resistance. Part 2: bridges. European Committee for Standardization, EN1998–2. 2005.
3. N.T.C. Technical regulations for the constructions. Italian Ministry of the Infrastructures, D.M. 17-01-2018. 2018.
4. Pan P, Zamfirescu D, Nakashima M, Nakayasu N, Kashiwa H. Base-isolation design practice in Japan: introduction to the post-Kobe approach. *J Earthq Eng*. 2005;9(1):147-171.
5. Itoh Y, Gu HS. Prediction of aging characteristics in natural rubber bearings used in bridges. *J Bridg Eng*. 2009;14(2):122-128.
6. Itoh Y, Gu HS, Satoh K, Yamamoto Y. Long-term deterioration of high damping rubber bridge bearing. *J Struct Mech Earthq Eng*. 2006;62(3):595-607.
7. Fuller KNG, Gough J, Thomas AG. The effect of low temperature crystallization on the mechanical behaviour of rubber. *J Polym Sci, Part B*. 2004;42(11):2181-2190.
8. Paramashanti, Itoh Y, Kitane Y, Gu HS. Long-term performance evaluation of high damping rubber bearings by accelerated thermal oxidation test. 2nd International Conference on Advances in Experimental Structural Engineering, Tongji University, Shanghai, China, December 2007; 4–6.
9. Paramashanti KY, Itoh Y, Kito S, Muratani K. Experimental investigation of aging effect on damping ratio of high damping rubber bearing. *J Struct Eng*. 2011;57A:769-779.
10. Cardone D, Gesualdi G, Nigro D. Effects of air temperature on the cyclic behavior of elastomeric seismic isolators. *Bull Earthq Eng*. 2011;9(4):1227-1255.
11. Higashino M, Hamaguchi H, Minewaki S, Aizawa S. Basic characteristics and durability of low-friction sliding bearings for base isolation. *Earthq Eng Eng Seismol*. 2003;4(1):95-105.
12. Tyler RG. Dynamic tests on PTFE sliding layers under earthquake conditions. *Bull New Zealand National Soc Earthq Eng*. 1977;10(3):129-138.
13. Dolce M, Cardone D, Croatto F. Frictional behavior of steel-PTFE interfaces for seismic isolation. *Bull Earthq Eng*. 2005;3(1):75-99.
14. McVitty WJ, Constantinou MC. *Property Modification Factors for Seismic Isolators: Design Guidance for Buildings MCEER-15-0005*. Buffalo, NY: MCEER; 2015.
15. Buckle IG, Kelly JM. Properties of slender elastomeric isolation bearings during shake table studies of a large-scale model bridge deck. Joint sealing and bearing Systems for Concrete Structures, American concrete institute, Detroit (Michigan) 1986; 1:247–269.
16. Vemuru VSM, Nagarajaiah S, Mosqueda G. Coupled horizontal–vertical stability of bearings under dynamic loading. *Earthq Eng Struct Dyn*. 2016;45(6):913-934.
17. Warn GP, Whittaker AS, Constantinou MC. Vertical stiffness of elastomeric and lead–rubber seismic isolation bearings. *J Struct Eng*. 2007;133(9):1227-1236.

18. Nagarajaiah S, Ferrell K. Stability of elastomeric seismic isolation bearings. *J Struct Eng*. 1999;125(9):946-954.
19. Constantinou M, Mokha A, Reinhorn A. Teflon bearings in base isolation. II: modeling. *J Struct Eng*. 1990;116(2):455-474.
20. Tsopelas PC, Constantinou MC, Reinhorn AM. 3D-BASIS-ME: computer program for nonlinear dynamic analysis of seismically isolated single and multiple structures and liquid storage tanks. Multidisciplinary Center for Earthquake Engineering Research, Buffalo, NY, Technical Report MCEER-94-0010. 1994.
21. FIP Industriale S.p.A. Catalogue S04: curved surface sliders. Padova, 2013; http://www.fipindustriale.it.
22. Kumar M, Whittaker AS, Constantinou MC. Characterizing friction in sliding isolation bearings. *Earthq Eng Struct Dyn*. 2015;44(9):1409-1425.
23. Quaglini V, Bocciarelli M, Gandelli E, Dubini P. Heating in sliding bearings for seismic isolation. *J Earthq Eng*. 2014;18(8):1198-1216.
24. Hamaguchi H, Samejima Y, Kani N. A study of aging effect on rubber bearings after about twenty years in use. 11th World Conference on Seismic Isolation, Energy Dissipation and Active Vibration Control of Structures, Guangzhou, China, November 2009; 17–21.
25. Van Engelen NC, Kelly JM. Retest of neoprene seismic isolation bearings after 30 years. *Struct Control Health Monit*. 2015;22(1): 139-151.
26. Kato M, Watanabe Y, Yoneda G, Tanimoto E, Hirotani T, Shirahama K, Fukushima Y, Murazumi Y. Investigation of aging effects for laminated rubber bearings of Pelham bridge. *Proc. of the 11th World Conference on Earthquake Engineering, Paper No. 1450, Acapulco, Mexico, Jun. 23–28*.1996.
27. Choun Y-S, Park J, Choi I-K. Effects of mechanical property variability in lead rubber bearings on the response of seismic isolation system for different ground motions. *Nucl Eng Technol*. 2014;46(5):605-618.
28. Gheryani MH, Razak HA, Jameel M. Dynamic response changes of seismic isolated building due to material degradation of HDRB. *Arab J Sci Eng*. 2015;40(12):3429-3442.
29. Bhagat S, Wijeyewickrema AC. Seismic response evaluation of base-isolated reinforced concrete buildings under bidirectional excitation. *Earthq Eng Eng Vib*. 2017;16(2):365-382.
30. Mazza F, Vulcano A. Nonlinear dynamic response of r.c. framed structures subjected to near-fault ground motions. *Bull Earthq Eng*. 2010;8(6):1331-1350.
31. Jalayer F, De Risi R, Manfredi G. Bayesian cloud analysis: efficient structural fragility assessment using linear regression. *Bull Earthq Eng*. 2015;13(4):1183-1203.
32. Pacific Earthquake Engineering Research Center. Pacific Earthquake Engineering Research Center database. http://ngawest2.berkeley.edu. 2014
33. Buckle IG, Constantinou M, Dicleli M, Ghasemi H. Seismic isolation of highway bridges. Special report, MCEER-06-SP07, Multidisciplinary Center for Earthquake Engineering Research, Buffalo, New York. 2006
34. Muramatsu Y, Nishikawa I. A study for the prediction of the long-term durability of seismic isolators. *Showa Electr Wire Rev*. 1995;45(1):44-49.
35. ASTM. *Standard Test Methods for Vulcanized Rubber and Thermoplastic Rubbers and Thermoplastic Elastomers-Tension*. American Society for Testing and Materials, D412; 1988.
36. Constantinou M, Whittaker AS, Kalpakidis Y, Fenz DM, Warn GP. Performance of seismic isolation hardware under service and seismic loadings. Technical report MCEER-07-0012, August 24, 2007. 2007.
37. Nelson W. *Accelerated Testing*. New York: J. Wiley & Sons; 1990.
38. Le Huy M, Evrard G. Methodologies for lifetime predictions of rubber using Arrhenius and WLF models. *Die Angewandte Makromolekulare Chemie*. 1998;261-262(1):135-142.
39. Mazza F. Advanced shear and axial laws of bearings in the nonlinear seismic analysis of r.c. buildings. Eleventh U.S. National Conference on Earthquake Engineering, June 25–29, Los Angeles, California. 2018
40. Kumar M, Whittaker AS, Constantinou MC. An advanced numerical model of elastomeric seismic isolation bearings. *Earthq Eng Struct Dyn*. 2014;43(13):1955-1974.
41. Fagà E, Ceresa P, Nascimbene R, Moratti M, Pavese A. Modelling curved surface sliding bearings with bilinear constitutive law: effects on the response of seismically isolated buildings. *Mater Struct*. 2016;49(6):2179-2196.
42. Naeim F, Kelly JM. *Design of Seismic Isolated Structures: From Theory to Practice*. New York, U.S.A: John Wiley & Sons Ltd; 1999.
43. Mazza F, Mazza M, Vulcano A. Base-isolation systems for the seismic retrofitting of r.c. framed buildings with soft-storey subjected to near-fault earthquakes. *Soil Dyn Earthq Eng*. 2018;109:209-221.
44. Mazza F, Vulcano A. Effects of the near-fault ground motions on the nonlinear dynamic response of base-isolated r.c. framed buildings. *Earthq Eng Struct Dyn*. 2012;41(2):211-232.
45. Shahi SK, Baker JW. An efficient algorithm to identify strong-velocity pulses in multicomponent ground motions. *Bull Seismol Soc Am*. 2014;104(5):2456-2466.

46. Mollaioli F, Lucchini A, Cheng Y, Monti G. Intensity measures for the seismic response prediction of base-isolated buildings. *Bull Earthq Eng*. 2013;11(5):1841-1866.

47. Mazza F, Labernarda R. Structural and non-structural intensity measures for the assessment of base-isolated structures subjected to pulse-like near-fault earthquakes. *Soil Dyn Earthq Eng*. 2017;96:115-127.

48. Jalayer F, Ebrahimian H, Milano A, Manfredi G, Sezen H. Analytical fragility assessment using unscaled ground motion records. *Earthq Eng Struct Dyn*. 2017;46(15):2639-2663.

49. Acunzo G, Pagliaroli A, Scasserra G. In-Spector: un software di supporto alla selezione di accelerogrammi naturali spettrocompatibili per analisi geotecniche e strutturali. *33° Convegno Nazionale GNGTS*, Bologna, Italy. 2014; 2:107–114.

How to cite this article: Mazza F. Effects of the long-term behaviour of isolation devices on the seismic response of base-isolated buildings. *Struct Control Health Monit*. 2019;e2331. https://doi.org/10.1002/stc.2331